Geophysical Journal International

Geophys. J. Int. (2021) **225,** 1874–1896
Advance Access publication 2021 February 13
GJI Marine Geosciences and Applied Geophysics

https://doi.org/10.1093/gji/ggab062

Evolution and properties of young oceanic crust: constraints from Poisson's ratio

M.J. Funnell[1], A.H. Robinson,[2] R.W. Hobbs[1] and C. Peirce[1]

[1]*Department of Earth Sciences, Durham University, Sciences Labs, Durham, DH1 3LE, UK. E-mail: matthew.funnell2@durham.ac.uk*
[2]*School of Ocean and Earth Sciences, University of Southampton, Waterfront Campus, European Way, Southampton SO14 3ZH, UK*

Accepted 2021 February 11. Received 2021 February 3; in original form 2020 October 16

SUMMARY

The seismic velocity of the oceanic crust is a function of its physical properties that include its lithology, degree of alteration and porosity. Variations in these properties are particularly significant in young crust, but also occur with age as it evolves through hydrothermal circulation and is progressively covered with sediment. While such variation may be investigated through *P*-wave velocity alone, joint analysis with *S*-wave velocity allows the determination of Poisson's ratio, which provides a more robust insight into the nature of change in these properties. Here we describe the independent modelling of *P*- and *S*-wave seismic data sets, acquired along an ∼330-km-long profile traversing new to ∼8 Myr-old oceanic crust formed at the intermediate-spreading Costa Rica Rift (CRR). Despite *S*-wave data coverage being almost four-times lower than that of the *P*-wave data set, both velocity models demonstrate correlations in local variability and a long-wavelength increase in velocity with distance, and thus age, from the ridge axis of up to 0.8 and 0.6 km s^{-1}, respectively. Using the *Vp* and *Vs* models to calculate Poisson's ratio (σ), it reveals a typical structure for young oceanic crust, with generally high values in the uppermost crust that decrease to a minimum of 0.24 by 1.0–1.5 km sub-basement, before increasing again throughout the lower crust. The observed upper crustal decrease in σ most likely results from sealing of fractures, which is supported by observations of a significant decrease in porosity with depth (from ∼15 to <2 per cent) through the dyke sequence in Ocean Drilling Program borehole 504B. High Poisson's ratio (>0.31) is observed throughout the crust of the north flank of the CRR axis and, whilst this falls within the 'serpentinite' classification of lithological proxies, morphological evidence of pervasive surface magmatism and limited tectonism suggests, instead, that the cause is porosity in the form of pervasive fracturing and, thus, that this is the dominant control on seismic velocity in the newly formed CRR crust. South of the CRR, the values of Poisson's ratio are representative of more typical oceanic crust, and decrease with increasing distance from the spreading centre, most likely as a result of mineralization and increased fracture infill. This is supported by borehole observations and modelled 3-D seismic anisotropy. Crustal segments formed during periods of particularly low half-spreading rate (<35 mm yr^{-1}) demonstrate high Poisson's ratio relative to the background, indicating the likely retention of increased porosity and fracturing associated with the greater degrees of tectonism at the time of their formation. Across the south flank of the CRR, we find that the average Poisson's ratio in the upper 1 km of the crust decreases with age by ∼0.0084 Myr^{-1} prior to the thermal sealing of the crust, suggesting that, to at least ∼7 Myr, advective hydrothermal processes dominate early CRR-generated oceanic crustal evolution, consistent with heat flow measurements.

Key words: Composition and structure of the oceanic crust; Controlled source seismology; Seismic tomography; Mid-ocean ridge processes.

1 INTRODUCTION

Oceanic crust is highly diverse in lithology and physical characteristics across a wide range of temporal and spatial dimensions. Its formation along the ∼65 000-km-long global ridge system occurs over full spreading rates (FSR) ranging from ∼10 to 150 mm yr^{-1}, and exhibits varying degrees of asymmetry that change over time (Müller *et al.* 2008). Crustal accretionary processes, which largely control lithology and structure, are considered to be dependent on the local spreading rate, and correlations are observed between FSR, crustal thickness and geochemistry (White *et al.* 1992; Bown & White 1994; Dick *et al.* 2003). Modelling of accretionary processes at fast, buoyancy-dominated spreading centres indicates magmatic input dominates, with faulting only generating small offsets, while at slower, stretching-dominated spreading centres, low degrees of magmatic input and high degrees of tectonic extension result in large-offset faulting (e.g. Buck *et al.* 2005; Howell *et al.* 2019). At the lowest FSR, ultraslow spreading centres (<20 mm yr^{-1} – Dick *et al.* 2003) are dominated by tectonic spreading (Buck *et al.* 2005) that exhumes, along detachment faults, large cross-sections of the lower crust and serpentinized mantle known as oceanic core complexes (Cann *et al.* 1997; Smith *et al.* 2006; MacLeod *et al.* 2009; Reston & Ranero 2011).

As newly formed oceanic crust migrates away from the ridge axis it cools and subsides (Stein & Stein 1992; Hasterok 2013), primarily as a result of heat loss through hydrothermal circulation (Stein & Stein 1994) and, as sedimentation increases, thermal conduction (Fisher *et al.* 2003). These processes alter the upper crust (Audhkhasi & Singh 2019) and effectively infill fractures, reducing porosity and permeability inherited at formation and during early development (Shaw 1994). Although this change is gradual, over time cracks are sealed and hydrothermal circulation becomes negligible. Ultimately, as an oceanic plate approaches a subduction zone, it migrates over the outer-rise, where bend-related stresses form new, or reactivate pre-existing, abyssal-hill faults (Ranero *et al.* 2003; Billen *et al.* 2007) that enable fluid circulation and facilitate renewed hydration and serpentinization of the crust and upper mantle (Ivandic *et al.* 2008; Grevemeyer *et al.* 2018b).

Investigations of oceanic crustal structure and composition, as well as understanding of their variation, are routinely based on determining seismic velocity, through 1-D profiles (e.g. Bratt & Solomon 1984; Collier & Singh 1998), 2-D profiles (e.g. Van Avendonk *et al.* 1998; Audhkhasi & Singh 2019; Peirce *et al.* 2019a,b; Wilson *et al.* 2019; Christeson *et al.* 2020; Davy *et al.* 2020) and 3-D tomographic grids (e.g. Toomey *et al.* 1990; Gregory 2018; Robinson *et al.* 2020; Simao *et al.* 2020), that have become more detailed through the use of greater numbers of instrumentation deployed at smaller spatial intervals and able to sample at higher temporal rates. These improvements in instrumentation, jointly with increased computational power and more complex modelling methods, have enabled increasingly high-resolution imaging of oceanic crustal structure. Both *P*- and *S*-wave velocity, *Vp* and *Vs*, respectively, are influenced by changes in rock porosity and composition. However, as a result of typically higher signal-to-noise ratios (SNR), lower phase ambiguity, and more extensive observation, *P*-wave arrivals are more commonly used to investigate rock properties. Differences in composition and varying porosity and crack aspect ratios within the crust (Shearer 1988; Wilkens *et al.* 1991) disproportionately affect *Vp* and *Vs*, altering the *Vp*/*Vs* ratio and, thus, also the effective Poisson's ratio (σ).

Both *Vp*/*Vs* and Poisson's ratios should be determined by independently modelling *Vp* and *Vs*, and either of these discriminate rock properties better than any other individual seismic attribute (Christensen & Salisbury 1975; Spudich & Orcutt 1980). For example, σ has been demonstrated to provide constraints on the nature and extent of fractures and cracking throughout the oceanic crust at various stages of its evolution (Shaw 1994; Christeson *et al.* 1997; Collier & Singh 1998), and also to discriminate between composition, as well as the magmatic and tectonic end-members of crustal formation (Christensen 1996, 2004; Grevemeyer *et al.* 2018a; Peirce *et al.* 2020).

The vertical velocity gradient, when used coincidently with depth-contextualized absolute values of *Vp*, has been demonstrated to differentiate between localized regions of basaltic crustal accretion, localized magmatism, and mantle exhumation processes at slow and ultraslow spreading centres (Harding *et al.* 2017; Grevemeyer *et al.* 2018b; Peirce *et al.* 2019a,b; Davy *et al.* 2020). However, Grevemeyer *et al.* (2018b) highlight that this approach fails to determine the extent of crust formed through magma-poor processes, as might be expected from observations of lower crustal thickness. Instead, a *Vp*/*Vs* ratio proxy is developed, discriminating between serpentinized peridotites with $Vp/Vs > 1.9$ ($\sigma > 0.31$) and mafic crust and dry mantle with $Vp/Vs < 1.9$ ($\sigma < 0.31$), that has subsequently been adopted (Peirce *et al.* 2019b) and slightly modified (*Vp*/*Vs* proxy of 1.85 – Peirce *et al.* 2020) to investigate accretionary processes at different spreading centres. These proxies are based on laboratory samples (e.g. Christensen, 1996, 2004; Carlson & Miller 1997), which demonstrate an increase in σ as a function of increasing degrees of peridotite serpentinization, whilst at lower degrees of bulk serpentinization, such as in differentiating between dry mantle and mantle that has been highly faulted, hydrated and serpentinized as a result of subduction-related bend-faulting (Ranero *et al.* 2003), the proxy of *Vp*/*Vs* ratio of 1.8 ($\sigma = 0.28$ – Grevemeyer *et al.* 2018b) has been applied.

The *Vp*/*Vs* and Poisson's ratios have also been observed to vary as a function of non-lithological controls, such as faulting and porosity. In newly formed oceanic crust, σ is found to be very high in the volcanic extrusives (0.48), where porosity can exceed 30 per cent (Collier & Singh 1998). Poisson's ratio in the uppermost crust also reduces both as depth increases into the intrusive dykes (porosity <5 per cent), and as the volcanic section ages (porosity <15 per cent – Pezard 1990; Detrick *et al.* 1994). A significant decrease in σ to 0.24 has been associated with the Layer 2/3 transition in young oceanic crust, which was initially suggested to result from quartz-rich lithologies (Spudich & Orcutt 1980) or crack orientation-related anisotropy (Fryer *et al.* 1989), despite limited supporting evidence from boreholes. Varying aspect ratio crack populations with depth were demonstrated to sufficiently control Poisson's ratio (Shearer 1988) and also reconcile borehole observations with theoretical models and geophysical data (Christeson *et al.* 1997). As oceanic crust evolves, the porosity and fractures generated during crustal formation become increasingly sealed as a function of age (Kolandaivelu *et al.* 2020), with observed values of Poisson's ratio in the upper crust decreasing until ∼60 Myr old (Shaw 1994), where they reach values typical for laboratory samples for gabbro ($\sigma \approx 0.28$ – Christensen 2004). Whilst the original model of Shaw (1994) implies that all fractures are sealed and hydrothermal circulation ceases by ∼60 Myr, continuing hydrothermal circulation has been observed at various sites >65-Myr-old (Von Herzen 2004), and in 106-Myr-old oceanic crust where the oceanic basement is morphologically raised (Fisher & Von Herzen 2005). Audhkhasi & Singh (2019) infer from seismic observations that hydrothermal circulation continues passively in oceanic crust >4 Myr old, and more locally when crustal age exceeds 15 Myr, suggesting

that porosity and fractures may remain sufficiently open to facilitate fluid flow in the oceanic crust even at full maturity.

In this study, we interpret new 2-D *Vp* and *Vs* models from a flowline-parallel profile acquired through oceanic crust formed at the Costa Rica Rift (CRR) in the Panama Basin, revisiting the *P*-wave model of Wilson *et al.* (2019) and extending it to mantle depth. This transect samples oceanic crust of 0–7 Ma, formed at varying half-spreading rates and, thus, with a varying dominance of magmatic input (Buck *et al.* 2005; Wilson *et al.* 2019). With independently derived *Vp* and *Vs* models, we determine Poisson's ratio along profile and apply this, with ground-truth provided by Ocean Drilling Program (ODP) borehole 504B (henceforth referred to as 504B for simplicity), to investigate crustal composition and porosity as a function of depth through the crust, age and rate and asymmetry of spreading at the time of formation. Finally, these controls on the geophysical crustal properties are compared with studies at other sites globally, and are considered in the context of heat flow to provide new insight into how the oceanic crust in the Panama Basin is evolving.

2 GEOLOGICAL AND TECTONIC CONTEXT

The Panama Basin is a bathymetrically restricted ocean basin located in the equatorial Pacific Ocean between 0–7°N and 78–90°W (Fig. 1a). The basin is bound by Central and South America to the north and east, and the Cocos and Carnegie Ridges to the west and south, respectively. Oceanic crust within the basin is formed along the Galapagos Spreading Centre (Klitgord & Mudie 1974), separating the Cocos Plate in the north from the Nazca Plate to the south (Hey 1977; Wilson & Hey 1995), and is subducted to the east along the Ecuador Trench (Aubouin *et al.* 1981). As these plates migrate over the Galapagos hotspot (Cleary *et al.* 2020), thickened crust of 12–19 km thick is generated, forming the Cocos, Carnegie and Malpelo Ridges in an orientation reflecting their host plate motions relative to the hotspot over at least the last ∼20 Myr (Hey 1977; Sallarès & Charvis 2003; NRR-MORVEL56; Argus *et al.* 2011).

While the Galapagos Spreading Centre (GSC) extends from the Galapagos Islands to the Panama Fracture Zone (PFZ), crustal formation occurs along discrete ridge segments separated by fracture zones (Fig. 1a). These are, from west to east: the GSC, which has a typical ridge crest topography (Klitgord & Mudie 1974) and is divided by an overlapping propagator at 87°30′W (Perram & Macdonald 1994); the Ecuador Ridge (ER); and the Costa Rica Rift (CRR), which comprises two segments with rift valley topography divided by a non-transform discontinuity (Buck *et al.* 1997; Lowell *et al.* 2020). Each of these spreading centres exhibits divergence rates that span the 'intermediate' spreading rate category (55–75 mm yr^{-1} FSR – Dick *et al.* 2003). The CRR, the focus of this study, has been active for at least 11 Myr (Lonsdale & Klitgord 1978), and over that time has demonstrated highly asymmetric spreading rates (Wilson & Hey 1995; Wilson *et al.* 2019), with half-spreading rates (HSR) ranging from ∼20 to >40 mm yr^{-1} (Wilson *et al.* 2019). These variations in spreading rate have been hypothesized to control crustal formation processes at the CRR, with slower rates resulting in increased faulting, and higher rates encouraging a greater dominance of magma generation (Wilson *et al.* 2019). Episodic magmatism on a decadal scale has been observed by repeated seismic reflection imaging of an ∼5-km-long axial magma lens, no more than ∼0.3 km wide (Buck *et al.* 1997; Lowell *et al.* 2020), with a microseismicity study indicating the likely presence of high-temperature hydrothermal circulation associated with it (Tary *et al.* 2021).

The evolution with age of CRR crust demonstrates a general increase in *P*-wave velocity, superimposed on the structural variability associated with changes in spreading rate (Wilson *et al.* 2019). This change with age is also coincident with an increase in observed conductive heat flow measured along flowline (Fig. 1b). The conductive heat flow measurements reach the theoretical heat flow curve, and thus 'basement sealing' at 7 Myr (Kolandaivelu *et al.* 2020), significantly earlier than the 65 ± 10 Myr average basement sealing age determined globally (Stein & Stein 1994). The rate of sedimentation in the basin is ∼40 m Myr^{-1}, with an ∼275 m succession imaged at 504B (Wilson *et al.* 2019), located ∼233 km (equivalent to ∼6.9 Myr) south of the CRR (Alt *et al.* 1996). The lithology, structure, and physical properties of the hydrothermally altered upper oceanic crust were also sampled at 504B to a depth of ∼1830 m below the basement (Alt *et al.* 1996). The volcanic extrusives were observed to extend ∼600 m below the sediment, followed by an ∼200-m-thick transition into sheeted dykes, which were sampled throughout the remaining ∼1000 m of the borehole. Reduction in electrical resistivity correlates with these lithological changes, with the apparent bulk porosity reduced from ∼14 to ∼8 per cent in the volcanic section, and to <2 per cent in the sheeted dykes (Pezard 1990). Furthermore, sonic log and sonobuoy (Collins *et al.* 1989) *P*-wave velocity was found to reflect these porosity variations, although the high velocity gradient and velocity exceeding 6.5 km s^{-1} led Detrick *et al.* (1994) to infer the onset of seismic Layer 3 approximately half-way through what was later sampled as sheeted dykes. More recent tomographic modelling of a 3-D seismic data set located at 504B supports these results, with porosity and mineralogy cited as the control on the Layer 2/3 boundary, and not the morphology of the gabbro-dyke transition (Gregory 2018).

3 DATA ACQUISITION

SAP_B, a coincident multichannel (MCS), wide-angle (WA), and synthetic aperture (SA) seismic profile was acquired during January–March 2015 as part of the OSCAR (*Oceanographic and Seismic Characterization of heat dissipation and alteration by hydrothermal fluids at an Axial Ridge*) project (Fig. 1 – Hobbs & Peirce 2015; Morales Maqueda 2015). This profile was one of three flowline-parallel profiles (SAP_A, SAP_B & SAP_C – Fig. 1) that connected two 3-D grid surveys; one located across the current CRR spreading centre (North Grid or NG – Robinson *et al.* 2020) and the other on ∼6.9 Myr old crust surrounding 504B (South Grid or SG – Gregory 2018), the latter providing direct lithological and downhole log constraint (e.g. Detrick *et al.* 1994; Alt *et al.* 1996; Carlson 2010). Magnetic data were acquired during phases of seismic shooting, and gravity and multibeam swath bathymetry data were acquired throughout the cruises on the RRS James Cook (JC114) and FS Sonne (SO238). These geophysical data sets are complemented by a range of heat flow (Kolandaivelu *et al.* 2020) and oceanographic data (e.g. Banyte *et al.* 2018a,b; Lowell *et al.* 2020) acquired during cruises JC112, JC113 and SO238.

SAP_B is ∼330 km long and runs from ∼40 km north (∼1.5-Myr-old crust) to ∼290 km south (>7-Myr-old crust) of the CRR spreading axis (Fig. 1b – Hobbs & Peirce 2015). Wilson *et al.* (2019) discuss the seismic structure and properties of the upper crust (sediment layer and oceanic crustal Layer 2) along SAP_B,

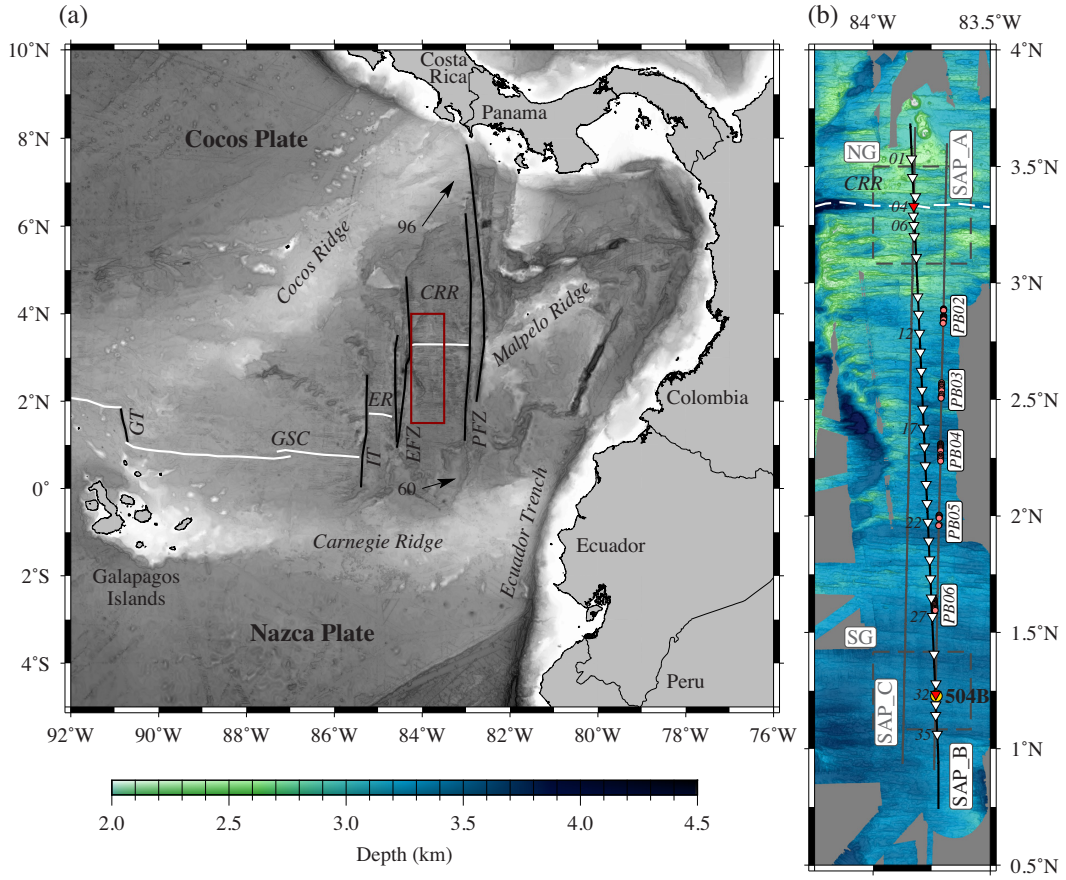

Figure 1. Bathymetric and tectonic map of the Panama Basin, bound by the Cocos and Carnegie Ridges and Central and South America. (a) GEBCO bathymetric map (GEBCO Compilation Group 2020) with white lines showing active spreading centres (GSC – Galapagos Spreading Centre; ER –Ecuador Ridge; CRR – Costa Rica Rift) and black lines showing transform faults and fractures zones (GT – Galapagos Transform; IT – Inca Transform; EFZ – Ecuador Fracture Zone; PFZ – Panama Fracture Zone). Red box shows the location of (b). (b) Swath bathymetry shaded by slope and with the CRR axis represented by the dashed white line. ODP borehole 504B (Alt *et al.* 1996) is indicated by a solid yellow circle. The black and grey lines correspond to the SAP profiles as labelled, with the inverted triangles, and associated numbers, representing OBSs deployed along SAP_B. The two dashed-grey boxes represent the footprints of two 3-D tomographic grids acquired (SG – Gregory 2018; NG – Robinson *et al.* 2020). The red-coloured OBS are those whose data is presented in Figs 2 and 3, located proximal to the CRR axis and 504B, respectively, and are those presented by Wilson *et al.* (2019). Locations of heat flow measurements acquired during OSCAR are shown by the orange circles, labelled according to acquisition set (see Kolandaivelu *et al.* 2020 and *cf.* Fig. 10).

and summarize the MCS, WA and SA data acquisition along profile. Here we extend the WA data analysis to uppermost mantle depth and resolve the whole crustal and upper mantle *P*- and *S*-wave velocity structure. In turn, we also calculate Poisson's ratio and use this to investigate the lithological and morphological characteristics of the crust, and determine any relationship with half-spreading rate, mode of formation and hydrothermal circulation and cooling. Wilson *et al.* (2019) modelled the shipboard magnetic data along only SAP_A and SAP_C to minimize violations of 2-D modelling assumptions (Fig. 1b), and so we include these spreading rate models here, alongside the model of Wilson & Hey (1995), to provide information on variations in spreading rate over time at the CRR.

Resolving the deeper crustal velocity structure requires identifiable arrivals at greater shot-receiver offsets than those picked and modelled by Wilson *et al.* (2019). An eight Sercel G-gun array (4280 in^3, 70.14 l) towed by the FS Sonne and fired at 60 s intervals (Hobbs & Peirce 2015) generated the arrivals picked and modelled in this study. WA seismic data were recorded on 32 of the 35 ocean-bottom seismographs (OBS) deployed at 5–10 km intervals along profile, with receiver spacings reduced at the profile ends where it traverses both 3-D grids (Fig. 1b). The OBSs recorded continuously on four channels (three orthogonal geophone components, one hydrophone) at either 250 or 500 Hz, depending on instrument type.

4 TRAVELTIME PICKING

For traveltime picking and assigning pick uncertainties, we followed the approach outlined in Wilson *et al.* (2019) and, to ensure consistency, we used their OBS locations on the seabed as determined by ray trace forward modelling of the direct arriving water-wave using *rayinvr* (Zelt & Smith 1992). Wilson *et al.* (2019) picked and modelled 5300 refracted *P*-wave arrivals turning in the upper and mid-crust (termed Pg arrivals), to a maximum shot-receiver offset of 31.6 km, but more typically to ∼20 km. We have expanded this *P*-wave traveltime data set, using both the hydrophone and vertical geophone components depending on SNR, for the 32 OBSs (example record sections for OBSs 04 and 32 are shown in Figs 2 and 3, with the locations of these OBSs shown on Fig. 1b), to include lower crust (also Pg) and upper mantle (termed Pn) turning arrivals at greater shot-receiver offsets, typically out to 50 km, but as far

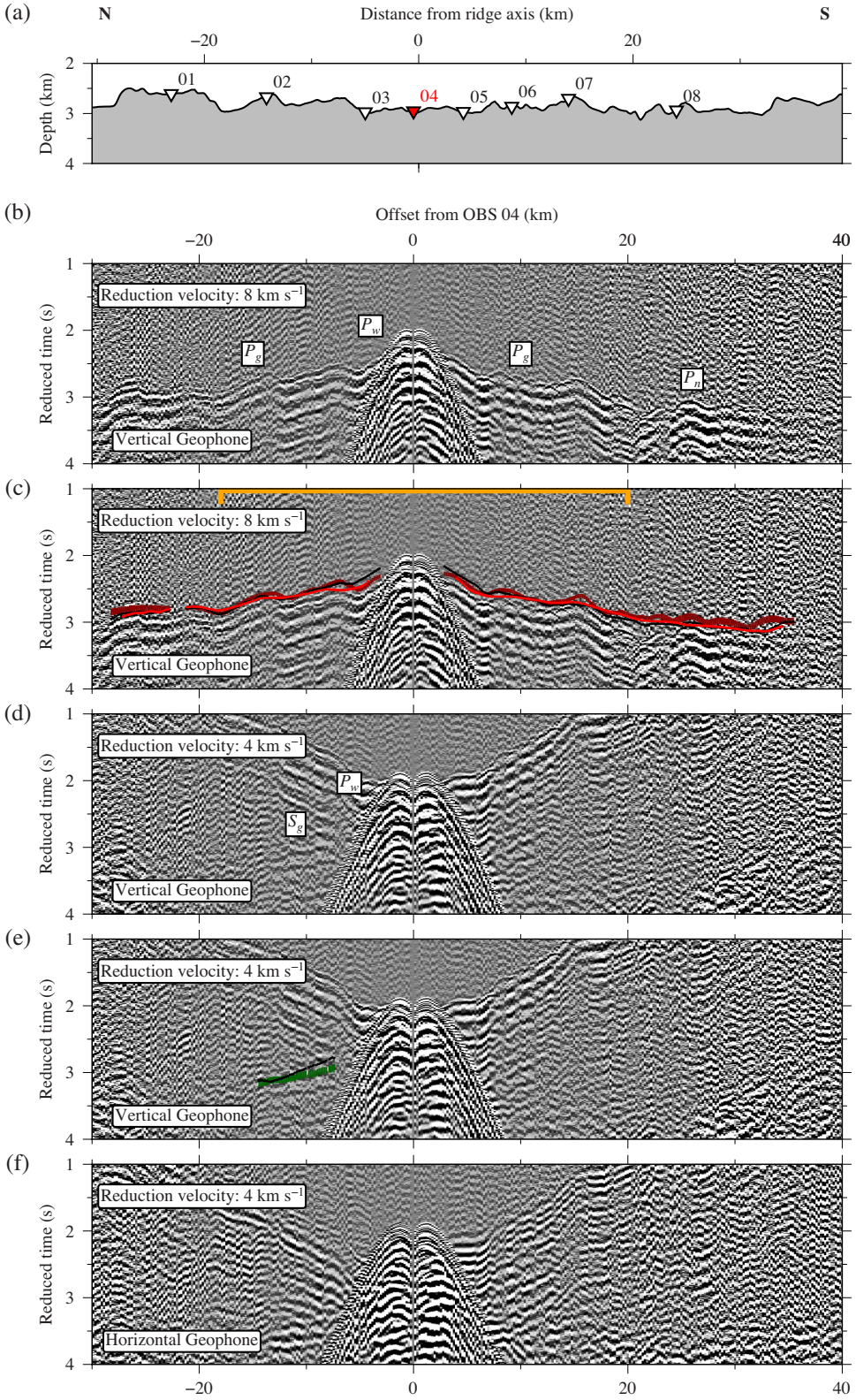

Figure 2. Example WA seismic data from OBS 04, located on the actively spreading Costa Rica Rift (Fig. 1b). (a) Bathymetry of the region surrounding OBS 04 (red inverted triangle), and its adjacent OBSs. (b) and (d) *P*-wave and *S*-wave arrivals recorded by the vertical geophone component plotted with a minimum phase bandpass filter (2-4-40-60 Hz). Annotated arrivals are labelled: Pw – direct water wave arrivals; Pg – crustal refracted *P*-wave arrivals; Pn – mantle refracted *P*-wave arrivals; Sg – crustal refracted *S*-wave arrivals. (c) and (e) *P*-wave and *S*-wave first arrival picks are denoted by vertical dark red and green bars, respectively, where bar height represents pick uncertainty. Assigned pick uncertainties are between 30 and 50 ms, typically increasing with offset and are higher for *S*-wave arrivals. Black lines in (c) and (e) represent modelled arrival times from the *FAST* inversions (see Figs 5 and 6, respectively). Red line in (c) is the modelled Pg and Pn arrivals from *rayinvr* forward modelling as in Fig. 7. Orange bar in (c) represents the range of first arrival offsets picked and modelled by Wilson *et al.* (2019). (f) Example horizontal geophone component for comparison.

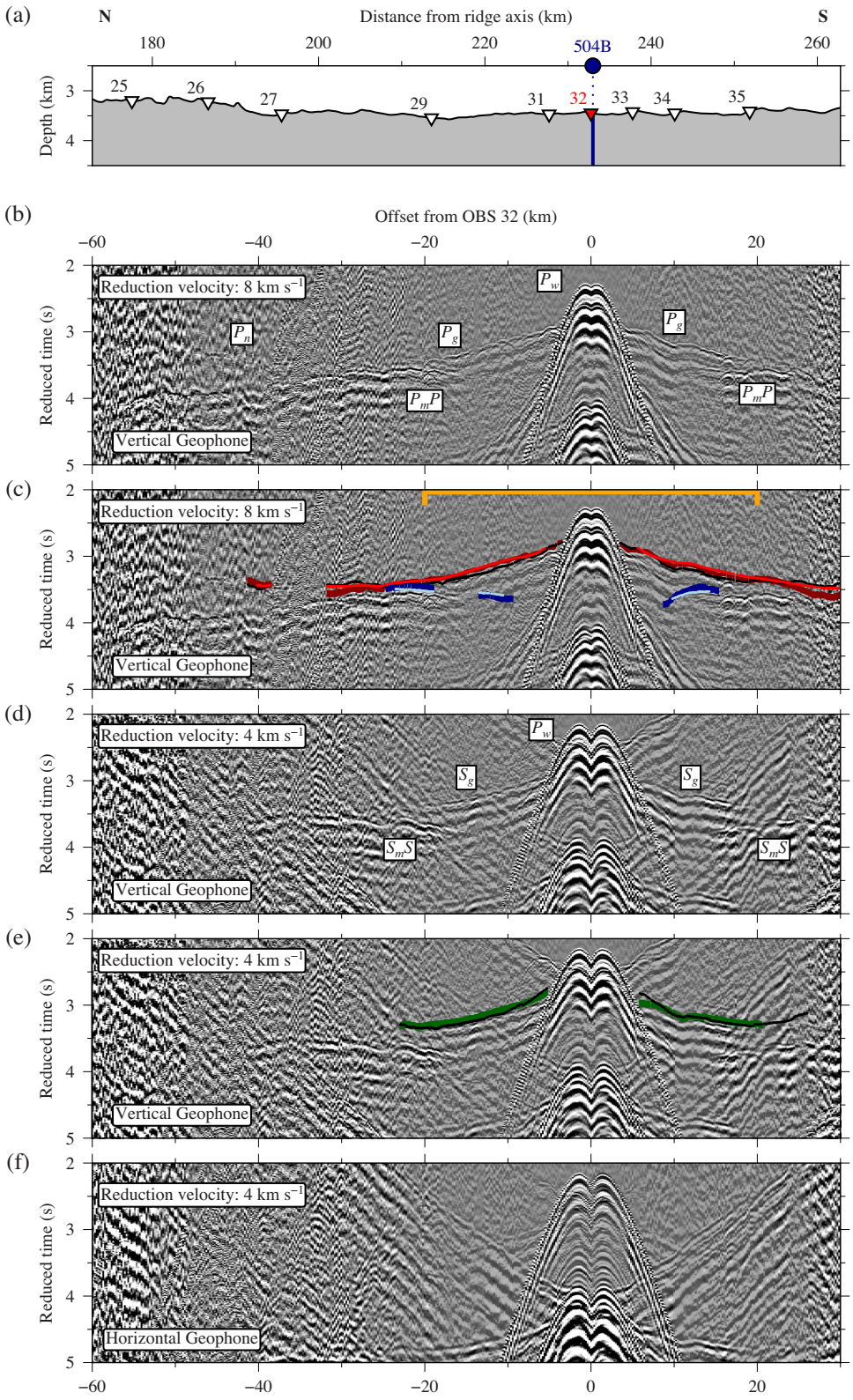

Figure 3. Example WA seismic data from OBS 32, located at borehole 504B in ∼6.9-Myr-old crust (Fig. 1b). (a) Bathymetry of the region surrounding OBS 32 (red inverted triangle) and its adjacent OBSs. ODP borehole 504B (Alt *et al.* 1996) is located by the blue circle with its extent sub-seabed shown by the blue line. (b) and (d) *P*-wave and *S*-wave arrivals recorded by the vertical geophone component plotted with a minimum phase bandpass filter (2-4-40-60 Hz). Annotated arrivals are labelled as described in Fig. 2, but with the inclusion of: PmP – Moho *P*-wave reflection (blue vertical bars representing pick uncertainty); and, SmS – Moho *S*-wave reflections (not picked or modelled due to large pick ambiguity), both of which are only typically observed on instruments located in more sedimented regions of SAP_B. Black lines in (c) and (e) represent modelled arrival times from the *FAST* inversions (see Figs 5 and 6, respectively). Red and light blue lines in (c) represent the modelled Pg and Pn jointly, and PmP arrivals, respectively, from *rayinvr* forward modelling as in Fig. 7. Orange bar in (c) represents the range of first arrival offsets picked and modelled by Wilson *et al.* (2019). (f) Example horizontal geophone component for comparison.

out as ∼80 km for a few of the instruments. In total, 15,908 *P*-wave refraction traveltime picks were made, including the original modelled set, representing a threefold increase. A fairly consistent density of ∼6.5 picks per shot was obtained along SAP_B (Fig. 4e), with there being generally more picks in areas with less sediment cover and vice versa. Error estimations are consistent with the original limited-offset pick data set, with the combined location and pick uncertainties set at ±30 ms for Pg arrivals (Wilson *et al.* 2019), increased to ±50 ms for Pn and PmP to account for the lower SNR at greater shot-receiver offsets (e.g. Figs 2c and 3c). Moho reflected *P*-wave arrivals (PmP) were also identified, resulting in ∼1700 further traveltime picks.

S-wave arrivals were picked using both the hydrophone and vertical geophone components in combination, to reduce the possibility of phase misinterpretation. We follow the phase nomenclature of Spudich & Orcutt (1980), and pick *S*-wave arrivals that we interpret as having propagated through the water column and sediments as *P* waves and through the basement as *S* waves, converting between *P* and *S* at the sediment-basement interface, or the water column-basement interface where sediment cover is negligible. The propagation mode and path of these arrivals are demonstrated in Fig. S1, along with the predicted traveltimes of these phases for OBS 32 (*cf.* Fig. 3), as well as additional traveltimes for *S* waves that do not convert to *P* waves at the sediment-basement interface. When coupled with the inherent complexities of picking arrivals within the acoustic wave train, such as interfering *P*-wave multiples and *S*-wave conversions (for example Figs 3d and e at offsets of 10–15 km cross-cutting the Sg arrival), the *S*-wave arrivals were only reliably and unambiguously picked to a maximum offset of ∼25 km from an instrument (Figs 2 and 3). As such, the *S*-wave picks are only attributed to arrivals solely turning within the crust (termed Sg). A total of 3904 *S*-wave traveltime picks were made along SAP_B, with the majority of these picks focused in regions with a combination of low basement roughness and increased sediment cover (Fig. 4). This suggests that *S*-wave transmission and recording is more controlled by basement structure and instrument coupling than their *P*-wave counterparts. Of particular note is the contrast between picks being made on the north flank of the CRR but not to its immediate south. Pick locations correlate with seabed morphological observations of reduced apparent tectonic extension and a greater surface cover of lava flows (Haughton *et al.* 2018). Due to the greater ambiguity in traveltime picking caused by the lower SNR and increased picking ambiguity, pick uncertainties were assigned at ±50 ms for all *S*-wave arrivals (Figs 2e and 3e). Table 1 summarizes the traveltime picks and error assignments.

5 TRAVELTIME INVERSION

Modelling of both *P*- and *S*-wave data sets was undertaken using *FAST* (Zelt & Barton 1998), which uses an inversion algorithm where traveltime residuals are minimized by iteratively updating a smooth velocity grid within the bounds of user-defined parameters. *FAST* was chosen as it is widely used, generates smooth velocity models independent of user bias, and is consistent with prior SAP_B upper crustal modelling by Wilson *et al.* (2019). The *P*- and *S*-wave data were inverted without any inter-dependence.

5.1 Initial model construction

The initial *P*- and *S*-wave velocity models were constructed on a uniform 0.1 × 0.1 km node grid by defining three sets of nodes to represent: (1) the water column; (2) the sediment cover; and (3) the crust and upper mantle combined. The velocity in each node above the sediment-basement interface, which includes the water column and sediment layer, remained fixed throughout the inversion. To adhere to the linearization assumption of *FAST* (Zelt & Barton 1998), that '*small perturbations to the starting model are determined*', the crust and upper mantle seismic velocities were defined to broadly match ridge-axis velocity compilations (e.g. White *et al.* 1992; Grevemeyer *et al.* 2018b).

In the initial *P*-wave (*Vp*) velocity–depth model, the velocity was set to increase from 4 km s^{-1} at the top basement interface to 6 km s^{-1} by 2 km below it, then increase with a shallower velocity gradient to 8.2 km s^{-1} at 12 km depth in model space, remaining fixed at 8.2 km s^{-1} below this (Fig. 5a). The initial *S*-wave (*Vs*) velocity–depth model was constructed to match the initial *Vp* model to the base of the sediment, with the picked Sg arrivals interpreted as having propagated through the water column and sediments as *P* waves and through the basement as *S* waves. From the top basement to the bottom of the model space, the initial *S*-wave velocity was obtained by conversion of the *Vp* initial model's velocity at the same depth using a *Vp*/*Vs* ratio of 1.7 (Fig. 6a), which represents a lower estimate for typical magmatically accreted oceanic crust (e.g. Carlson & Miller 1997; Christensen 2004; Grevemeyer *et al.* 2018a). This scaling factor was chosen to fit the observation that oceanic crust formed under a broadly magmatic regime at the CRR (Buck *et al.* 2005; Wilson *et al.* 2019), and also because it generates an initial *Vs* model that does not break the linearization assumption of *FAST*, that only small perturbations from the starting model are determined.

5.2 Inversion

Prior to inversion, a full range of inversion parameters was tested to determine initial start points such that modelling artefacts were minimized, whilst producing the highest resolution achievable from the traveltime data distribution. The parameters tested (see Table 2) include: S_z, which controls the relative amount of horizontal and vertical smoothing where a value of 0 eliminates vertical smoothing; α, which trades off fitting the smallest perturbation constraints ($\alpha = 0$) with the smoothest constraint equations ($\alpha = 1$), and; λ_0 and λ, which are the initial and subsequent trade-off parameters that control how *FAST* weights data misfit relative to the constraint equations, where λ is controlled by a reduction factor through each non-linear inversion iteration (Zelt & Barton 1998). Further to this, a range of other inversion starting models was tested including, for example, smooth models with a simple linearly increasing velocity from the top basement interface to the bottom of the model space (Fig. S2). Inversion of these alternative starting models resulted in either a failure to converge on a final model with an appropriate statistical misfit or models with artefacts (e.g. Figs S2b and c, which used the same modelling parameters as that set out in Table 2) caused by the starting model not conforming to the linearization assumptions of *FAST* (Zelt & Barton 1998). Inversion cell size primarily controlled resolution and artefacts introduced. For the *P*-wave inversion, a cell size of 1.5 km laterally and 1.0 km vertically was selected based on the testing. Following a single set of five non-linear iterations, a final *P*-wave model (henceforth *Vp model*) was produced for the full crust and uppermost mantle (Fig. 5b). This model has an average traveltime root mean square (RMS) misfit of 69 ms ($\chi^2 = 3.1$), reduced from 261 ms for the initial model (Fig. 5a). Alternative inversions using

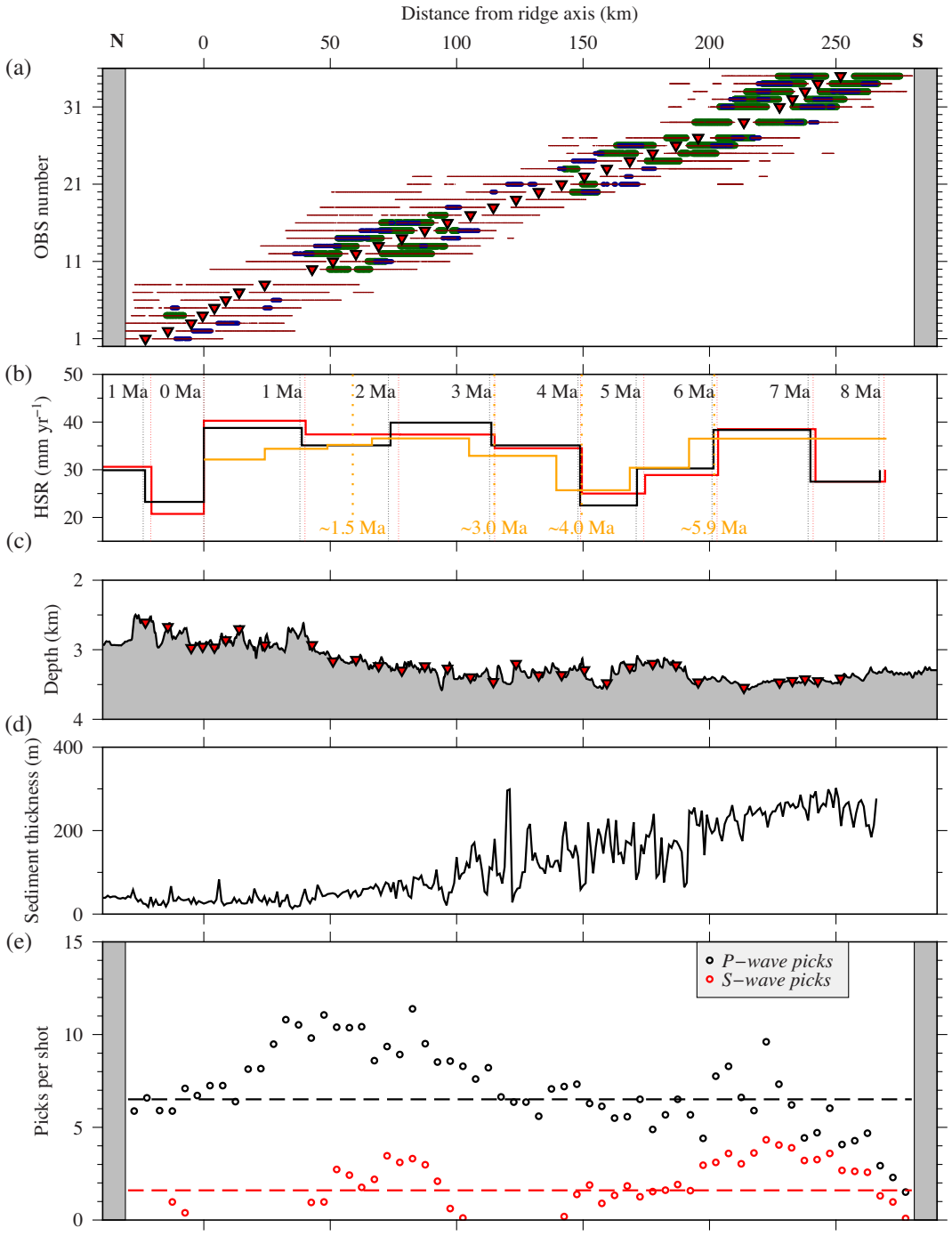

Figure 4. Summary of traveltime picks, by instrument, with distance along SAP_B. (a). Pick colours in (a) match those assigned in Figs 2 and 3, where red dots are *P*-wave refractions (Pg and Pn), blue dots are *P*-wave reflections (PmP), and green dots are *S*-wave refractions (Sg). Red triangles in (a) and (c) represent OBS locations along profile. Grey bands at the profile ends of (a) and (e) represent regions where no shots were fired and, thus, picks are absent. Note the broad correlation between low degrees of basement roughness (more constant sediment thickness) and increased *S*-wave picks along profile. (b) Modelled half-spreading rates (Wilson *et al.* 2019), along SAP_A (red line) and SAP_C (black line), and from Wilson & Hey (1995 – orange line and text) demonstrating variability along flowline (see Fig. 1 for locations). (c) Bathymetry along profile for comparison. (d) Sediment thickness along profile determined from the SAP_B MCS data (Wilson *et al.* 2019). (e) Number of *P*- and *S*-wave picks per shot within 5-km-along profile bins as indicated by black and red dots, respectively. On average, there are 6.5 picks per shot for *P*-wave arrivals, and 1.5 picks per shot for *S*-wave arrivals (shown by the dashed lines), demonstrating the reduced propagation of *S*-wave energy through the subsurface and the additional uncertainties in picking *S*-wave arrivals.

smaller inversion cell sizes, either following single or multiple sets of five iterations, consistently introduced ray path-focused velocity artefacts, despite in some cases further reducing the traveltime misfit.

Inversion of the *S*-wave data was undertaken following the same method as the *P*-wave data, with an aim of maintaining consistency in parameters between the two independent inversions (see Table 2). The final *S*-wave model (henceforth the *Vs model* – Fig. 6b) reduces

Table 1. Summary of traveltime picks and uncertainties, with statistical misfit for the *FAST Vp model* (Fig. 5), *FAST Vs model* (Fig. 6), and the *rayinvr Vp models* (Fig. 7).

Phase	Picks		FAST *Vp* model			FAST *Vs* model			rayinvr *Vp* model (5 km-thick crust)			rayinvr *Vp* model (6 km-thick crust)		
	N	Unc. (ms)	*N*	T_{RMS} (ms)	χ^2	*N*	T_{RMS} (ms)	χ^2	*N*	T_{RMS} (ms)	χ^2	*N*	T_{RMS} (ms)	χ^2
Pg	8226	20	15 908	69	3.1	-	-	-	7840	64	4.6	8211	56	3.5
Pn	7539	50				-	-	-	7064	119	5.7	6384	112	5.0
PmP	1727	50	-	-	-	-	-	-	1727	90	3.3	1727	53	1.1
Sg	3904	50	-	-	-	3904	63	1.6	-	-	-	-	-	-

the RMS misfit from 246 ms for the initial model to 62 ms, corresponding to $\chi^2 = 1.6$. This good fit was achieved irrespective of the considerably fewer Sg traveltime picks and despite the lack of picks in certain model regions and at mantle-turning offsets (Fig. 4e). The absence of Sg traveltime picks, particularly in regions of rough basement topography and reduced sediment cover, resulted in no model recovery at offsets >15 km to the north of the CRR, as well as between 0–40 km and 110–130 km to the south of the CRR (Fig. 6).

5.3 Resolution testing

Checkerboard testing of both velocity models was undertaken to determine the scale of resolvability of velocity anomalies throughout the 2-D model space (Zelt & Barton 1998). Checkerboard patterns were applied to each final model with a ±5 per cent velocity anomaly, and synthetic traveltimes calculated for the location of each observed traveltime pick. Random Gaussian noise was then added, with the user-defined pick uncertainties used as the one standard deviation misfit. The synthetic traveltimes were inverted using each of the final velocity models in turn as the initial model, and with the same inversion parameters (Table 2). The degree of recovery of the input checkerboard anomaly was then appraised using the semblance, with a value of ≥0.7 (Zelt 1998) regarded as well recovered. Checkerboard testing was undertaken over a range of horizontal (5–20 km) and vertical (1–5 km) scales and, for each anomaly scale, checkerboards were tested at all possible half-cell size shifts within the model space, following Zelt (1998). By inversion of checkerboards with different cell shifts, and the averaging of the semblance grids calculated for each, artefacts caused by anomaly polarity and cell boundaries are removed enabling model resolvability to be more objectively quantified (Zelt 1998; Zelt & Barton 1998).

For the *Vp model*, the smallest recoverable ±5 per cent anomaly checkerboards have a 15 × 2 km cell size to ∼6 km depth, although typically only in model regions with high instrument density, such as at the CRR and around 504B (Fig. 5d). No significant recovery of the checkerboard was found with checkerboard anomalies of 1 km vertical cell size. Recovery of the velocity structure deeper in the model space, to ∼8 km depth and as far as ∼250 km south of the CRR, is only achieved by checkerboards with cells that are at least 20 × 3 km in size (Fig. 5c).

The accuracy and robustness of the recovered velocity anomaly can be further tested by comparing the *Vp model* with the *OBS inversion model* presented by Wilson *et al.* (2019 – fig. 7). The only region where the *OBS inversion model* (Wilson *et al.* 2019) notably outperforms the *Vp model* is in the upper 0.5 km of the crust. This results from Wilson *et al.* (2019) adopting a modelling approach that enhances the resolution of shallow, small-scale, velocity anomalies for the investigation of the Layer 2A/B boundary, whereas the modelling process we adopt facilitates the resolution of deeper and larger-scale velocity structure.

Checkerboard testing of the *Vs model* achieved recovery of 20 × 2 km sized cells with ±5 per cent checkerboard anomalies, although only in two regions where the oceanic basement is relatively smooth (Wilson *et al.* 2019): between 45 and 100 km, and 170–260 km south of the CRR (Fig. 6d). As with the 15 × 2 km cell size checkerboard tests for the *Vp model*, resolvability above a 0.7 semblance threshold was only achieved to 6–7 km depth (2-3 km sub-basement) for this checkerboard size, equivalent to the upper-mid oceanic crust (Grevemeyer *et al.* 2018b; White *et al.* 1992). Increasing the vertical checkerboard cell size to 20 × 3 km for the *Vs model* tests did not achieve any significant improvement in the resolvability of deeper velocity structures, indicating that the majority of the refraction turning depths were shallower than ∼7 km (Fig. 6c). This depth is insufficient to image the Moho and upper mantle with *S* waves, which is not surprising given the absence of unequivocally identified mantle turning arrival picks. However, with the larger vertical cell size, recovery of the velocity anomaly was improved along profile, most notably beneath the CRR and where the basement topography is rougher between 140 and 170 km south of the CRR.

6 MODEL INTERPRETATION

6.1 *Vp* model

The *Vp model* exhibits a generally smooth and artefact-free velocity structure, with *Vp* generally increasing with distance from the spreading centre at all depths in the model space (Fig. 5b). The significant exception to this is an anomalously low-velocity region, at >8 km depth, between 50 and 100 km south of the CRR that is situated below the 0.7 semblance contour, and thus is most likely a modelling artefact generated by poor resolvability in this region of the model. Within Layer 2, *Vp* increases from 4.2 to 6.1 km s^{-1} at the CRR to ∼5.0–6.5 km s^{-1} at 504B (Fig. 5e). The inversion cell size and lack of small-scale feature resolution prevents the *Vp model* from distinguishing the lower velocity of the volcanic extrusives comprising the uppermost crust (Fig. 5), and thus also the high velocity gradient to the basaltic dykes (>2 s^{-1}; Gregory 2018), as was achieved by the inclusion of synthetic aperture traveltime picks by Wilson *et al.* (2019) in their inversion of the upper crust. However, the 1-D *Vp*-depth profile taken through the model at 504B (Fig. 5e) demonstrates a comparable velocity range to that observed in the ∼1800-m-deep borehole logs (∼4.5–6.5 km s^{-1}; Alt *et al.* 1996), with only the lower velocity of volcanic extrusives absent from the model. At the CRR, the *Vp model* has a very close fit to the *inversion model* of Robinson *et al.* (2020) throughout the ∼4 km sub-basement sampled by both models. In Layer 3, *Vp* also increases with distance from the CRR, consistently displaying

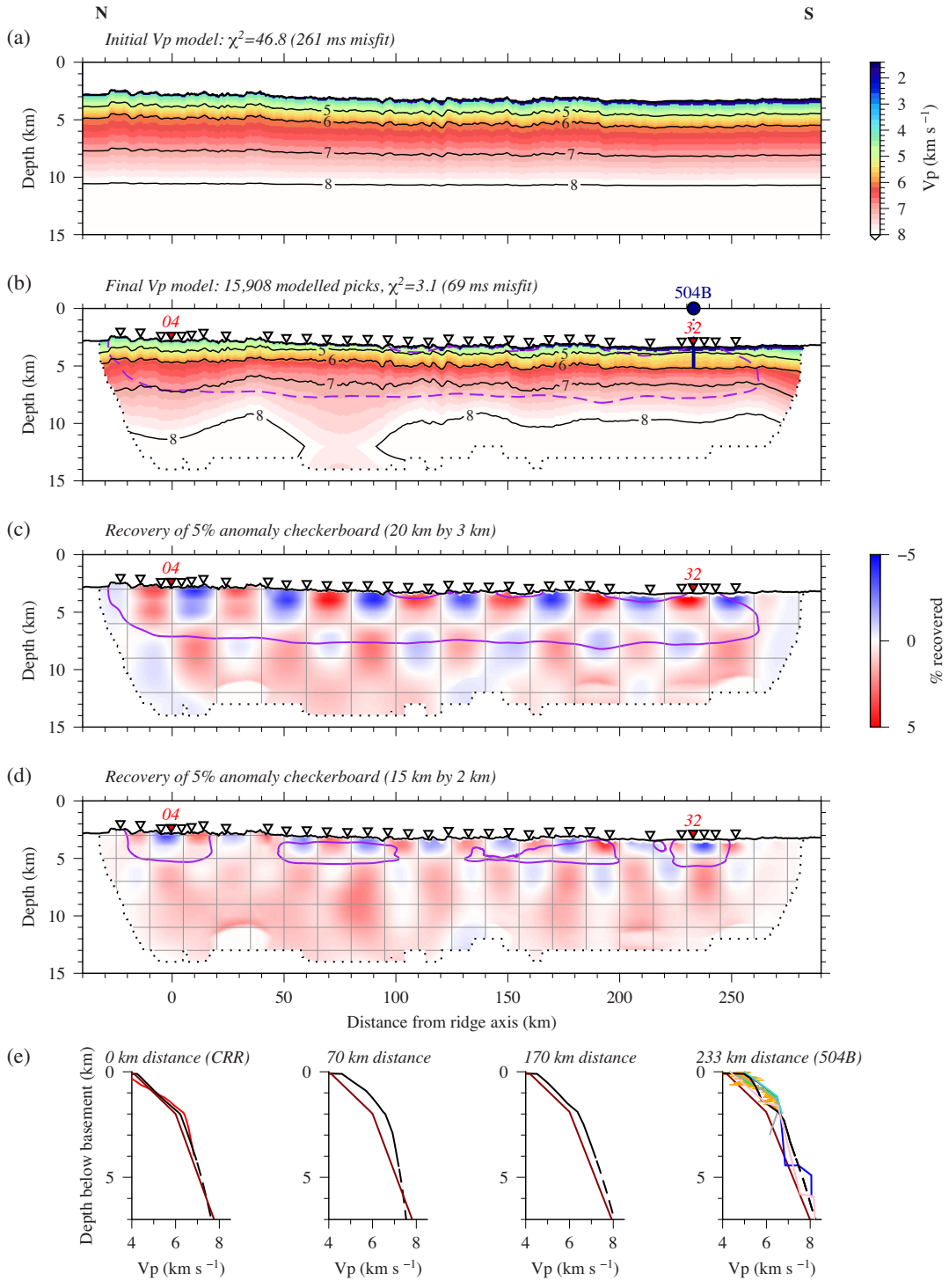

Figure 5. *P*-wave inversion modelling and checkerboard testing. (a) Initial *P*-wave velocity model, with fixed water column and sediment layer velocities based on that used by Wilson *et al.* (2019), below this velocity increases to 8.2 km s^{-1} at 12 km model depth. (b) Final *Vp model* with a RMS misfit of 69 ms corresponding to a $\chi^2 = 3.1$. The dashed purple line represents the 0.7 semblance contour as in part (c). 504B drill site location, and depth below seabed sampled along SAP_B are indicated by the vertical blue line. The extent of model ray coverage is delimited in (b)–(d) by a dotted black line, and regions with no coverage are masked. The purple line represents the 0.7 semblance (Zelt 1998; Zelt & Barton 1998) threshold contour of all checkerboard cell half-shifts tested for the presented anomaly size, with gridlines indicating the original checkerboard structure. OBS locations are indicated by inverted triangles, where the red numbered OBSs have data presented in Figs 2 and 3. (c) and (d) Recovery of a ±5 per cent velocity anomaly checkerboard using the same modelling geometry, picks (Table 1), and parameters (Table 2) as in the inversion of the *Vp model*. (e) 1-D velocity–depth profiles sampled from the initial model (red) and final *Vp model* (black) at specified distances from the CRR. Black dashed lines indicate where the velocity model resolvability falls below 0.7, as shown in (c). Bright red 1-D velocity–depth profile at 0 km distance (CRR) is the *on-axis profile* from Robinson *et al.* (2020). Equivalent profiles for the upper crustal model of Wilson *et al.* (2019) are shown in grey. Other 1-D velocity–depth profiles include the 504B well log (orange), upper crustal models (green and turquoise) from Detrick *et al.* (1994), inferred crustal thickness model (blue) from Collins *et al.* (1989) and the *rayinvr Vp model* (pink – Fig. 7).

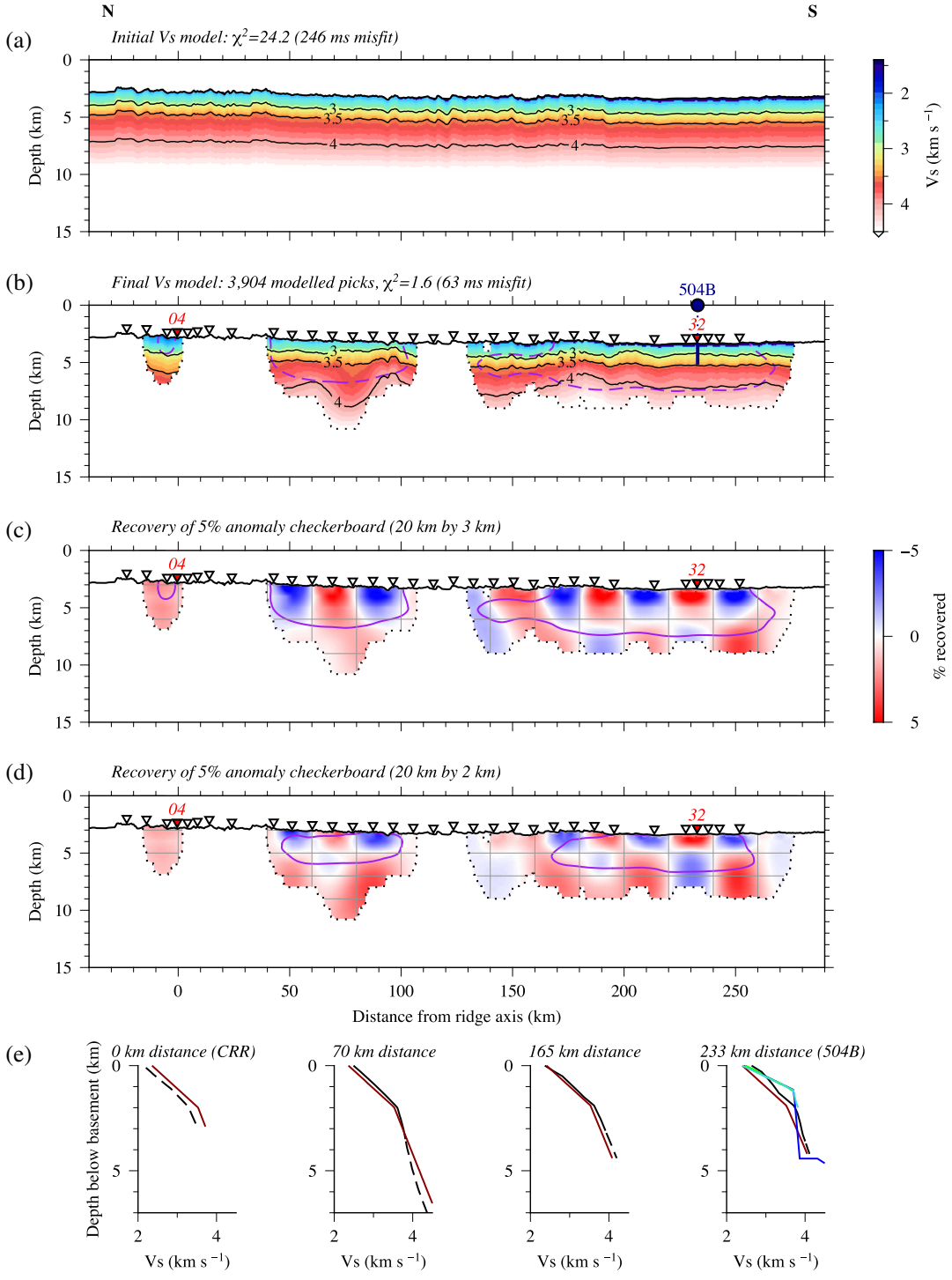

Figure 6. [um2] *S*-wave inversion modelling and checkerboard testing. (a) Initial *S*-wave velocity model created by scaling the velocity sub-sediment layers of the initial *P*-wave model by a factor of 1.7. (b) Final *Vs model* with a RMS misfit of 63 ms corresponding to a $\chi = 1.6$. The dashed purple line represents the 0.7 semblance contour as in part (c). 504B drill site location, and depth below seabed sampled along SAP_B are indicated by the vertical blue line. The extent of model ray coverage is delimited in (b) – (d) by a dotted black line, and regions with no coverage are masked. The purple line represents the 0.7 semblance (Zelt 1998; Zelt & Barton 1998) threshold contour of all checkerboard cell half-shifts tested for the presented anomaly size, gridlines indicate the original checkerboard structure. OBS locations are indicated by inverted triangles, where the red numbered OBSs have data presented in Figs 2 and 3. (c) and (d) Recovery of a ±5 per cent velocity anomaly checkerboard using the same modelling geometry, picks (Table 1), and parameters (Table 2) as in the inversion of the *Vs model*. Reduced profile coverage compared to the *Vp final model* is largely a function of the lower arrival signal-to-noise ratio and thus number of *S*-wave traveltime arrivals picked, as demonstrated in Fig. 4. (e) 1-D velocity–depth profiles sampled from the initial model (red) and final *Vs model* (black) at specified distances from the CRR. Black dashed lines indicate where the velocity model resolvability falls below 0.7, as shown in (c). Other 1-D velocity–depth profiles from 504B include the upper crustal models (green and turquoise) from Detrick *et al.* (1994), and inferred crustal thickness model (blue) from Collins *et al.* (1989).

Table 2. Summary of inversion parameters for the *Vp model* and *Vs model* (after Zelt & Barton 1998). Note that the inversion parameters were kept the same for both velocity models to maintain consistency of modelling approach.

Inversion parameter	Value
S_z	0.25
α	1
λ_0	100
λ reduction factor	1.414
Forward node spacing	0.1 km
Inversion cell size (horizontal)	1.5 km
Inversion cell size (vertical)	1 km

a steeper velocity–depth profile and reaching a higher velocity at shallower depth relative to the top basement. Lower crustal velocity structure lies at the limit of resolvability within the model space, while contours that are typically taken to represent the Moho (e.g. 7.8 or 8.0 km s^{-1}) lie significantly below the limit of this resolvability. As a result of this resolution limit, the lower crustal and upper mantle velocity structure, including the Moho, are investigated and tested separately by forward ray tracing of the associated traveltime picks and modelling of the density structure along SAP_B (e.g. Figs 7 and 8).

The velocity variation along the flowline *Vp model* is best demonstrated by subtraction of a 1-D velocity–depth profile sampled at the zero-age CRR (Fig. 9b). This approach enables differentiation between structurally controlled lateral velocity variability, such as horizontal stepping across a fault, and other processes such as crustal evolution and different oceanic crust formational mechanisms (Wilson *et al.* 2019). From ∼25 km south of the CRR, *Vp* is elevated throughout the crust, significantly increasing by 0.4–0.8 km s^{-1} within Layer 2 (∼2 km sub-basement) between 50 and 120 km. The seismic velocity is less than 0.4 km s^{-1} faster than at the ridge axis in Layer 2 between 120 and 200 km, before increasing again to between 0.4 and 0.8 km s^{-1} faster as far as ∼260 km south of the CRR. In contrast to the Layer 2 velocities which are highly variable with distance from the ridge axis, Layer 3 (2–4 km sub-basement) remains more consistent, only significantly increasing up to 0.4 km s^{-1} faster than zero-age crust by ∼200 km offset, and 0.4–0.6 km s^{-1} faster to the edge of model resolvability at 260 km south of the CRR.

Wilson *et al.* (2019 – fig. 7c) present a comparable figure, based on their high resolution *FAST final inversion model* and, whilst generated using different modelling parameters that resolve different wavelength features, the broad-scale velocity variations occur at very similar distances from the CRR. For example, the most notable similarities are the extent of higher velocity regions within Layer 2 relative to zero-age crust between 50–120 and 200–260 km south of the CRR. This further indicates that whilst there are minor differences between the Wilson *et al.* (2019) *FAST final inversion model* and our *Vp model* (Fig. 5), the velocity variations along profile are controlled primarily by the geology and do not result from the different modelling parametrizations adopted.

6.2 *Vs* model

The *Vs model* also demonstrates a relatively smooth and artefact-free velocity structure that broadly increases with distance from the ridge axis, except for a low-velocity region >6 km deep between 60 and 90 km south of the CRR (Fig. 6b). As with the *Vp model*, *Vs* increases within Layer 2, from ∼2.3 to 3.5 km s^{-1} at the CRR, to 2.6–3.8 km s^{-1} at 504B (Fig. 6e). Comparable increases in *Vs* are also observed in Layer 3, reaching a high of ∼4.2 km s^{-1} at 504B.

Vs variability along the profile, normalized to a 1-D *Vs*-depth profile sampled through the zero-age CRR crust, reflects the increasing velocity with distance from the ridge axis (Fig. 9c). Despite the more laterally limited ray coverage across the model space, similar observations can be made to those for the *Vp model*. Relative to the CRR axis, in Layer 2 along-flowline, *Vs* is higher by 0.2–0.6 km s^{-1} between 40 and 100 km, and between 200 and 260 km south of the ridge axis. *Vs* is not significantly faster (<0.2 km s^{-1}) between 130 and 150 km, but does increase by up to 0.4 km s^{-1} between 150 and 200 km. The extent of these regions of higher and lower velocity differences relative to CRR axis is consistent with that of the *Vp model*, although slightly reduced in magnitude.

These coincident variations between the independently derived *Vp* and *Vs models*, albeit of differing magnitudes, indicate that whatever the primary control is on one of these properties (i.e. lithological, alteration, fracturing, or porosity), it is also likely the primary influence on the other. A caveat to this is that the *Vs model* lacks ray coverage along the entire length of the profile and, as such, there may be regions of the unsampled subsurface that do not follow the apparent trend indicated by these models. It is also worth noting that the model offset ranges with no or limited ray coverage (Fig. 4), generally correspond to regions with rough basement topography (Wilson *et al.* 2019), and are those in which the *Vp model* indicates relatively low velocity increase compared to zero-age crust (Fig. 9b).

6.3 Poisson's ratio

Poisson's and *Vp*/*Vs* ratios have been used to investigate differences in the extent and nature of porosity (e.g. Spudich & Orcutt 1980; Collier & Singh 1998), as well as lithology and degree of alteration resulting from crustal formation and deformation processes (Christensen 1996; Grevemeyer *et al.* 2018a). While Poisson's and *Vp*/*Vs* ratios are both used, here we use σ to describe the relationship and correlation along SAP_B, but cite the equivalent *Vp*/*Vs* ratio where appropriate to enable comparison with previous studies.

With the *P*- and *S*-wave crustal velocity structures both well resolved and independently derived, the *Vp* and *Vs models* were integrated to determine σ along SAP_B (Fig. 9d). As the σ *model* is a function of both the *Vp* and *Vs models,* it is masked in regions of no ray coverage in both source models and, similarly, the 0.7 semblance contour encompasses only regions where both models are deemed resolvable. As such, σ is not determined between 20 and 40 km to the north, and 0–40, 110–130 and beyond 270 km to the south of the CRR. To enable direct comparison with investigations from other spreading centres (e.g. Grevemeyer *et al.* 2018a; Peirce *et al.* 2020), the $\sigma = 0.31$ contour (*Vp*/*Vs* = 1.9), is also marked on Fig. 9(d). Grevemeyer *et al.* (2018a) identified $\sigma = 0.31$ (*Vp*/*Vs* = 1.9) as a proxy to differentiate exhumed serpentinized mantle ($\sigma > 0.31$), from magmatically accreted basaltic crust ($\sigma < 0.31$), at the ultraslow Mid-Cayman spreading centre in the Cayman Trough.

Along SAP_B, where resolved, σ varies between 0.22 and 0.34, typically exhibiting higher values closer to the CRR and at shallower depths beneath the basement (Fig. 9d). The highest value of σ anywhere in the model lies between 0 and 20 km to the north of the CRR, reaching $\sigma = 0.34$ in the upper ∼500 m sub-basement. At these model offsets, σ reduces with increasing depth, reaching ∼0.30 at 1.5 km below basement, before increasing again to $\sigma > 0.31$ over

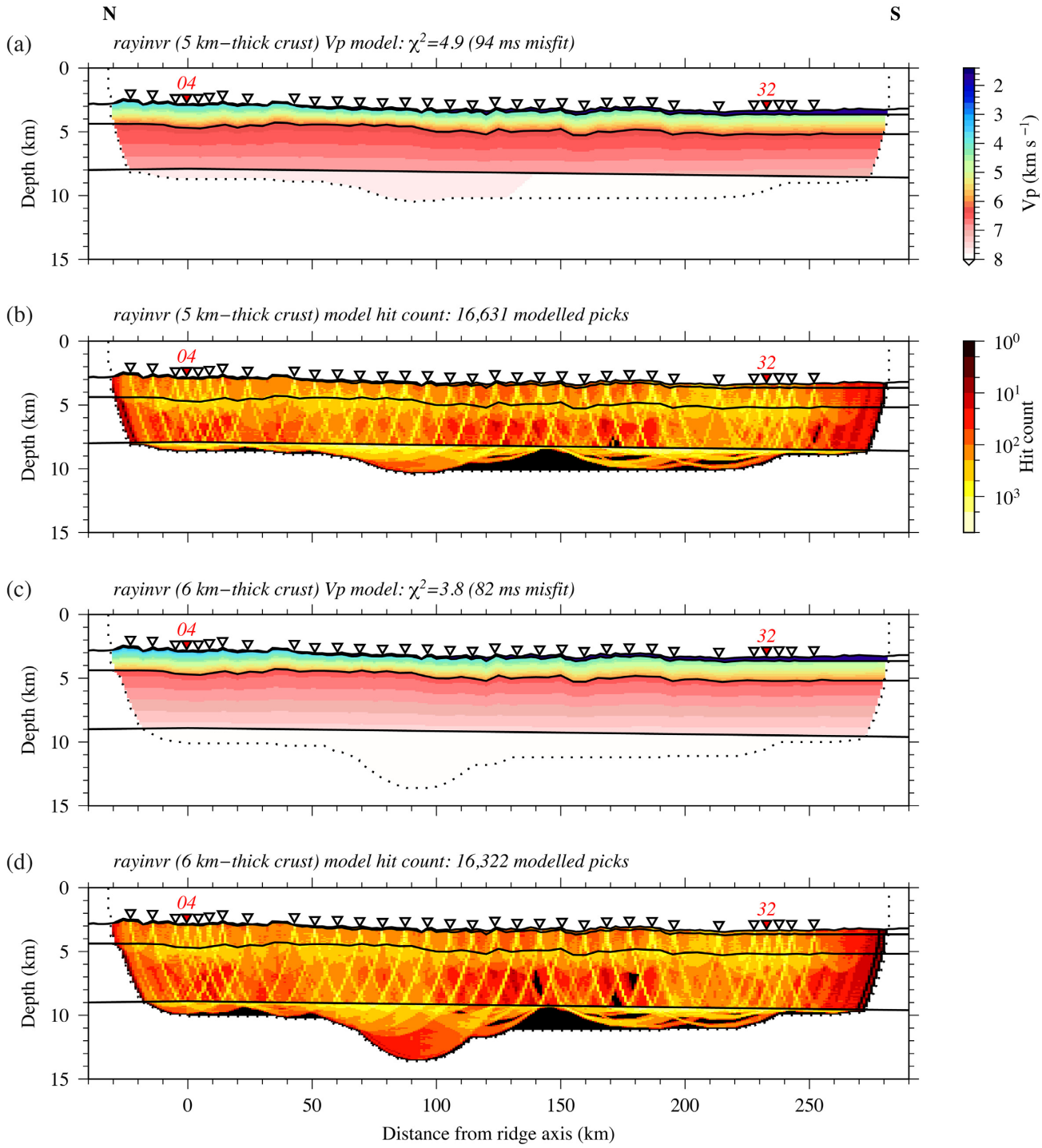

Figure 7. Ray trace modelling (*rayinvr* – Zelt & Smith 1992) to constrain crustal thickness. (a) Velocity model and (b) hit count, of a best-fit thin (∼5 km-thick) crust. (c) Velocity model and (d) hit count, of a best-fit normal (∼6-km-thick) crust. For both models, the water and sediment column, and uppermost layer of the oceanic crust are extracted and simplified from the *FAST Vp model* (Fig. 5b). The lower crust and uppermost mantle velocities are varied at no more than four nodes along-profile to maintain model simplicity and optimize the fit between the observed and modelled arrivals. The extent of model ray coverage is delimited in (a)–(d) by a dotted black line, and regions with no coverage are masked. OBS locations are indicated by inverted triangles, where the red numbered OBSs have data presented in Figs 2 and 3.

∼2 km in depth. South of the CRR, lower values of σ are determined between 40 and 90 km, and with less consistent vertical variability. From 40 to 70 km south of the CRR, σ generally decreases with depth (0.32–0.28), but from 70 to 90 km, this trend is reversed and σ increases below the basement interface (0.29–0.32). A region of anomalously low σ (0.22–0.26) is observed at 90–100 km from the CRR, resulting from a relatively high *Vs* at these offsets. This feature coincides with a large basement fault. However, the magnitude and location of this anomaly suggest that it may be a modelling artefact caused by low ray coverage (pick density – Fig. 4) in the *Vs model*

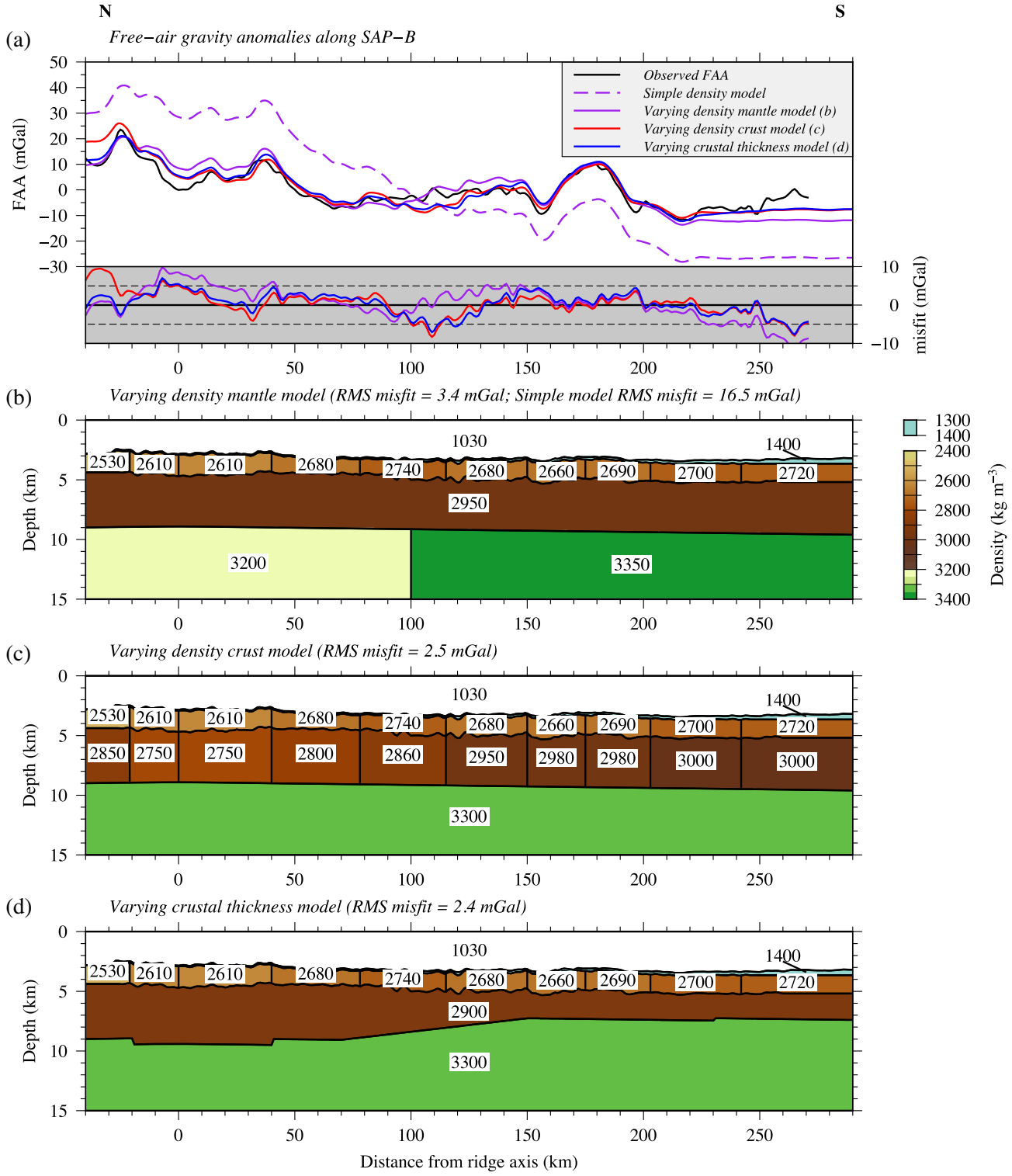

Figure 8. Gravity modelling along SAP_B based on the *FAST Vp model* and the 6-km-thick crust *rayinvr Vp model* (Figs 5 and 7, respectively). (a) Observed ship-derived FAA, normalized to 0 mGal, compared with the FAA calculated from the models presented in (b)–(d). Coloured lines represent models as described in the key. RMS misfit between the observed and varying density modelled FAA is presented below in the grey bar, with matching line colours. (b) *Varying density mantle model* comprises the same layers as the *simple density model*, but the *simple density model* mantle consists of a single unit with density 3300 kg m^{-3}. (c) *Varying density crust model*, with the lower crust subdivided laterally to fit the observed gravity anomaly. (d) *Varying crustal thickness model*, with the lower crust and upper mantle densities kept constant across the model and the depth of the crust-mantle boundary varied. In all models, densities are annotated in kg m^{-3}.

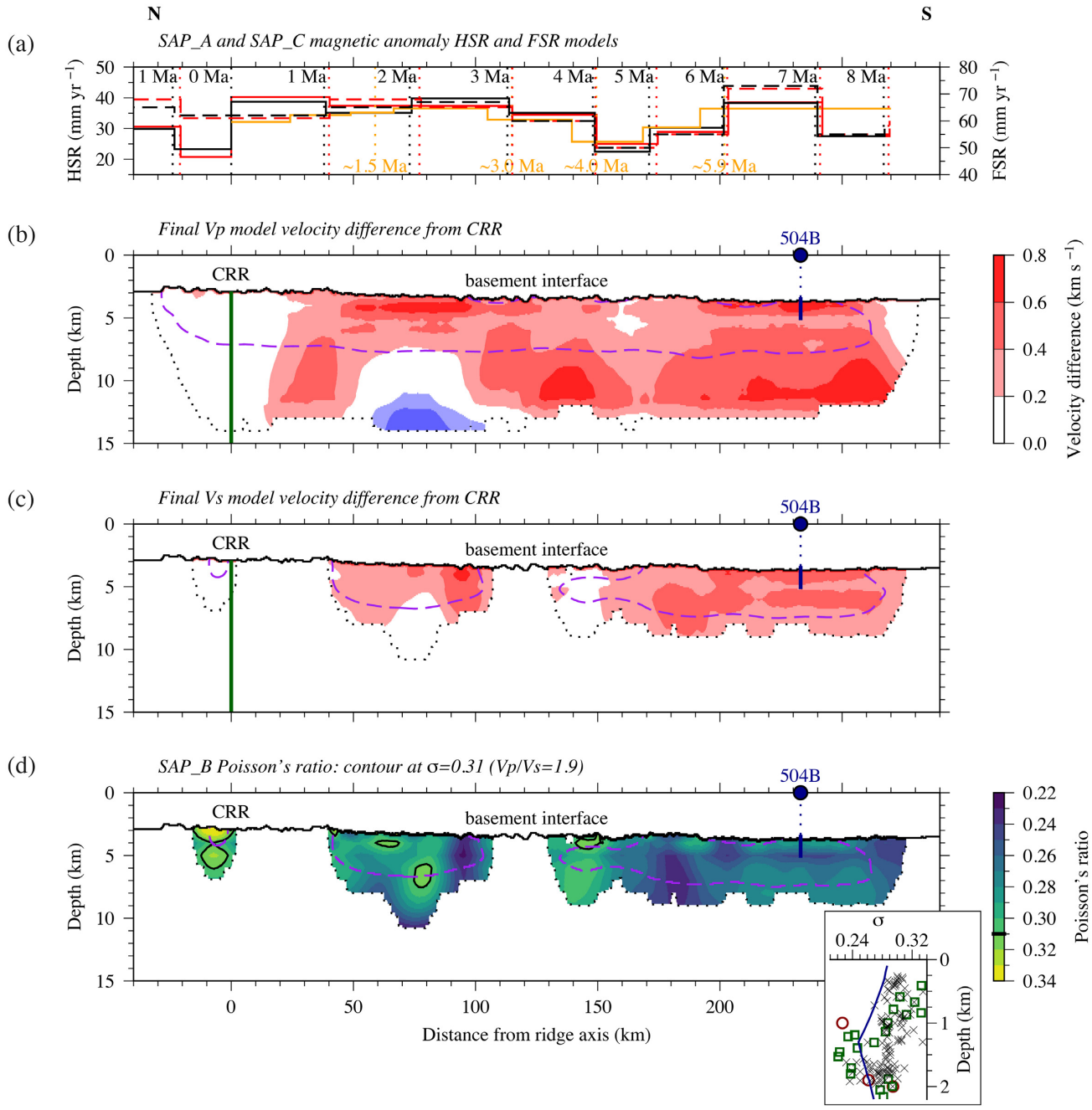

Figure 9. 2-D seismic velocity and related geophysical property variations along flowline (*cf.* Fig. 1b). (a) Half-spreading rate (HSR – solid line) and full-spreading rate (FSR – dashed line) models determined by Wilson *et al.* (2019) for the SAP_A (red) and SAP_C (black) magnetic data, and by Wilson & Hey (1995 – orange line and text). (b) and (c) Variations in the final velocity models relative to a 1-D velocity profile at the CRR (green line) taken from the basement interface. The models are masked by ray coverage. Purple dashed line is the 0.7 semblance contour for the 20 × 3 km checkerboard anomaly in Figs 5 and 6, respectively. (d) Poisson's ratio derived from the final velocity models masked by ray coverage, with the 0.7 semblance contour overlain, only where both velocity models achieve that condition. The $\sigma = 0.31$ ($Vp/Vs = 1.9$) contour is superimposed to demonstrate where the model exceeds this threshold, to indicate possible metamorphosed lithologies assuming a primarily lithological control on Poisson's ratio (Grevemeyer *et al.* 2018a). Inset: Comparison of Poisson's ratio against depth below basement at 504B for the SAP_B Poisson's ratio model (blue line) with laboratory-derived values from samples taken at 504B (black crosses – Iturrino *et al.* 1995), and seismic profile-derived models taken at other sites of young oceanic crust (green squares – Spudich & Orcutt 1980; red circles – Au & Clowes 1984).

at these offsets. Furthermore, the low-Poisson's ratio anomaly is laterally small, ~10 km wide, and thus falls below the minimum lateral width (20 km) of velocity anomalies that were found to be resolvable in the *Vs model* through checkerboard testing (Figs 6c and d). Poisson's ratio is further reduced throughout the southernmost portion of the model (130–270 km south of the CRR), with values between 0.23 and 0.31. Throughout most of this region, σ is reduced between 1 and 2 km sub-basement to 0.24–0.27, before generally increasing to ~0.27 for the lowermost 2 km of the recovered model space.

7 CRUSTAL THICKNESS

Through the modelling of the *Vp* and *Vs* data sets with *FAST*, velocity structure is well-resolved in the upper and lower oceanic crust along SAP_B. However, due to the absence of mantle refracted arrival picks in the *S*-wave data set (Sn), and the limited number in the *P*-wave data set (Pn), the Moho depth and upper mantle seismic velocity structure are either below the limit of resolution or entirely unconstrained in the *Vp* and *Vs* models, respectively (Figs 5 and 6). To provide constraint on the crustal thickness along SAP_B, we forward ray trace the *P*-wave refraction picks (15 908 Pg and Pn, combined) used in the *Vp model*, along with a further 1727 Moho reflection (PmP) picks.

The ray tracing was undertaken using a layered velocity model in *rayinvr* (Zelt & Smith 1992), which was constructed from the top down, using the same water column and sediment layer velocities and thicknesses as in the *FAST* initial model (Fig. 5a). The upper crustal layer is defined by the 6.0 km s^{-1} contour from the *Vp model* (Fig. 5b) as the layer's lower boundary, and a lateral velocity gradient from 3.2 to 4.5 km s^{-1} is imposed along the 330-km-long layer upper boundary to simplify the velocity model structure while maintaining consistency with the inversion *Vp model* (Figs 5 and 7). Below the upper crustal layer, the velocity model prioritizes structural simplicity, and is optimized to minimize the misfit between the observed and modelled traveltime picks. This simplification is necessary as the lowermost crust, Moho and upper mantle are sparsely sampled by PmP and Pn picks (Table 1), so small lateral variations as modelled in the *FAST Vp model* are not resolvable, although, importantly, long-wavelength consistency is maintained between models (Figs 5 and 7). Furthermore, *rayinvr* is less able to model significant sharp lateral velocity variations than *FAST*, so the model simplification also minimizes potential modelling artefacts. Two end-member models were considered for the lower crustal and upper mantle velocity structure, with a trade-off between crustal velocity and thickness: (1) a full crust that is thin with a lower velocity gradient and bulk velocity (~5 km thick on average – Figs 7a and b); and (2) a full crust of more typical thickness with a higher velocity gradient and bulk velocity (~6 km thick on average – Figs 7c and d). The thinner (~5 km thick) crust model, which is founded on the 4.5-km-thick crust indirectly inferred by Collins *et al.* (1989), achieved a minimum model misfit of $\chi^2 = 4.9$. Comparatively, the more typical (~6-km-thick) crust model (as assumed in Wilson *et al.* 2019; Robinson *et al.* 2020) was able to achieve a slightly improved total model misfit of $\chi^2 = 3.8$, with a notable reduction in the misfit of the Moho reflection (PmP) phase picks ($\chi^2 = 1.1$, compared with $\chi^2 = 3.3$ in the thin-crust model – Table 1).

Both ray tracing models achieve a worse statistical fit than the *Vp model,* which results from the increased simplification of crustal structure to a minimal number of layers with velocities defined at between only one and four nodes laterally for each layer. While we expect more variability in Moho structure than the linear gradient in depth with offset from the CRR as presented, our *rayinvr Vp models* (Fig. 7) demonstrate that the oceanic crust formed at the CRR better fits the observed traveltime data with an average thickness closer to ~6 km than the thinner (~5 km thick) determination of Collins *et al.* (1989). Further, crustal thicknesses of ~4.5 km, as indirectly inferred by Collins *et al.* (1989), are expected only to be formed where the spreading rate is ultraslow-to-slow (FSR <20 mm yr^{-1} – Dick *et al.* 2003). Oceanic crust formed at the CRR is modelled to have formed exclusively at intermediate spreading rates between 45 and 70 mm yr^{-1} (Wilson & Hey 1995; Wilson *et al.* 2019), which also suggests that a thin crust is unlikely. As a non-unique inverse problem, there are numerous possible solutions to the modelled data set that may be obtained by trading off the bulk lower crustal seismic velocity, velocity gradient and Moho depth in determining the average crustal thickness along SAP_B. Resolving these various attributes more robustly, and with a finer degree of lateral variability, requires a greater density of lower crustal and upper mantle-sampling arrival traveltimes picks that can be modelled.

8 GRAVITY

8.1 Modelling

To further independently test the validity of the velocity models and as a check of the forward ray traced crustal thickness estimate, the free-air gravity anomaly (FAA) along SAP_B was modelled and compared to the observed ship-acquired FAA (Fig. 8). A simple layered initial density model was created by extracting the 6.0 km s^{-1} contour from the *Vp model* in areas with ray coverage and, taking it to represent the lower boundary for the upper crust, combining it with the predetermined water column and sediment layer thicknesses (Wilson *et al.* 2019). The lower boundary for the lower crust was defined in the density models by the Moho depth from the preferred 6-km-thick crust *rayinvr Vp model* (Fig. 7c), as the *FAST Vp model* (Fig. 5) was unable to adequately resolve velocity structures at these depths. Typical densities for seawater (1030 kg m^{-3}), pelagic sediments in the Panama Basin (1400 kg m^{-3} – Karato & Becker 1983), and uppermost mantle (3300 kg m^{-3}) were assigned to their respective layers. The upper crust was subdivided laterally into 1 Myr blocks, as defined by Wilson *et al.* (2019) and enabled by the resolution of the *Vp model*, and the average velocity within each block was converted to density using the standard upper oceanic crustal relationship of Carlson & Raskin (1984). The average crustal layer velocities from the *Vp model* result in an average density of the upper (Layer 2) oceanic crust of 2680 kg m^{-3}, which lies within calculated density ranges from studies at other oceanic crustal sites (e.g. Carlson & Raskin 1984, and references therein) as well as the average densities of basaltic (2730 ± 90 kg m^{-3}) ophiolite samples (Carlson & Raskin 1984). For the lower crust, where *Vp model* resolution is insufficient to robustly constrain the lowermost crust, the density was set as 2950 kg m^{-3} to fit with models from previous studies as well as gabbroic (2830–2950 ± 70 kg m^{-3}) ophiolite samples (Carlson & Raskin 1984). The resulting simple density model (Fig. 8b) produces a gravity anomaly with a long-wavelength misfit compared to the observed data (Fig. 8a), with the modelled FAA higher than observed at the north end, and lower than the observed at the south end of SAP_B. The long-wavelength misfit could be resolved by either decreasing the crustal thickness or increasing layer densities with distance from the CRR.

First, variation in the mantle was investigated as this is least constrained by the seismic modelling. A good fit could be achieved by dividing the mantle layer into two distinct blocks (Fig. 8b), with a lateral density difference of 150 kg m^{-3} decreasing from 3200 kg m^{-3} at the CRR to 3350 kg m^{-3} beyond 70 km south of the CRR. This model in itself is not geologically plausible, but demonstrates how a gradation in mantle lithology or temperature along flowline could account for the long-wavelength FAA misfit. We note that Wilson *et al.* (2019) calculated that thermal maturity could contribute an ~25 mGal long-wavelength regional shift over

the length of SAP_B, with slight variations dependent on FSR at the time of accretion.

Although the crust to Layer 3 depth is well constrained by the seismic modelling, gravity modelling is non-unique and so other possible approaches to resolving the misfit between the calculated and observed FAA were also investigated by laterally varying the density structure with age within the crust itself (Fig. 8c). A good fit (RMS misfit = 2.5 mGal) could equally well be achieved by subdividing the lower crustal layer laterally in the same manner as the upper crust, and assigning densities that increase southwards. However, whilst all the assigned crustal densities fit within observed range (Carlson & Raskin 1984), to minimize the misfit the densities would need to increase by 200 kg m^{-3} in the upper crust and 250 kg m^{-3} in the lower crust between 0 and 290 km distance from ridge axis. We note that if the crust is thinner than the ∼6 km thickness determined by our *rayinvr model* then even greater density differences are required in the crust to achieve the same degree of fit to the observed FAA.

Finally, by fixing the *Vp model*-constrained upper crustal densities, and setting lower crust and upper mantle density values to 2900 and 3300 kg m^{-3}, respectively, within the typical ranges for these layers/units, the effect of varying crustal thickness on the modelled FAA was also investigated (Fig. 8d). A good statistical fit (RMS misfit = 2.4 mGal) to the observed FAA could be achieved if the crust–mantle boundary shallows by ∼2 km over the ∼250 km sampled by SAP_B south of the CRR. However, varying the crustal thickness alone, and to such a significant degree, is inconsistent with the *rayinvr Vp model* crustal structure, which required a largely invariant crustal thickness to achieve a fit in all modelled cases (Fig. 7). Further, the extent of crustal thinning required to fit the FAA exceeds that which is geologically plausible in a setting where ultraslow spreading rates are not observed.

In each of these approaches to minimizing the FAA misfit, the upper crust is consistent with the *Vp model* result, and either density increases with crustal age from the CRR or the crust thins significantly, resulting in good statistical fits of between 3.4 and 2.4 mGal RMS misfit. We prefer the varying density crust model (Fig. 8c) as it is the only model that is consistent with the *rayinvr Vp model* and is founded on a geologically plausible principle, and will henceforth be referred to as the *density model*. We also note that this does not, however, preclude limited aspects of the other models contributing to the total observed FAA.

8.2 Interpretation

The *Vp model*-derived *density model* generates a gravity anomaly that closely replicates the short wavelength variations of the observed FAA (Fig. 8). The large-scale structure is of a fairly constant, ∼6 km-thick oceanic crust, underlain by mantle of a typical density. Within the upper crust, the individual 1 Myr-segments reflect the structure of the *Vp model* (Fig. 5) on which it is based, as density varies with distance from the CRR. Within the upper crust there are general trends of regions having higher density if they are older or formed during periods of increased HSR. The lower crustal density structure, which is not based on any seismic constraint other than for the depth of the Moho (Fig. 7), demonstrates an increase in density with distance (age) from the CRR, but no correlation to HSR. We interpret these changes to be controlled by the formational and ageing processes of the oceanic crust, which have varying density as a function of initial lithology, and increase through alteration and the infilling of porosity.

9 DISCUSSION

Each of our models presented here illuminate a different aspect of the nature and variability in oceanic crustal structure along SAP_B, from its point of formation at the CRR to ∼7 Myr old crust where it is sampled by 504B. Both the *Vp model* and *Vs model* demonstrate increasing seismic velocities with distance from the CRR (Figs 5, 6 and 9) and are supported by long-wavelength increases in density as indicated by the *density model* (Fig. 8). Superimposed on this long-wavelength variability is the correlation between the upper crustal seismic velocity and density with the rate of spreading at the time of formation, which, as highlighted by Wilson *et al.* (2019), serves as a proxy for the magmatic fraction of formation (Buck *et al.* 2005). Together, the *Vp model* and *Vs model* result in a *Poisson's ratio model* (Fig. 9d) that indicates a general decrease in σ with distance from the CRR at all resolvable model depths, implying a significant control on these varying physical properties is the evolution of the oceanic crust over time through changes to the lithology and structure (e.g. faulting and fractures).

Borehole 504B, which is located ∼233 km south of the CRR ridge axis along SAP_B, provides geophysical and geological ground-truth through its sampling and geophysical logging of ∼7-Myr-old crust formed at the CRR. Downhole measurements of compressional wave velocity at 504B are quite variable, ∼5 ± 1 km s^{-1} in the upper ∼0.6 km, but increase to >6 km s^{-1} below 1.0 km sub-basement (Detrick *et al.* 1994). The *Vp model* (Fig. 5) broadly reflects this velocity profile, with a *Vp* of 5.0 km s^{-1} at the top of the crustal section, increasing to 6.0 km s^{-1} by 1.5 km sub-basement, and matching the ∼6.5 km s^{-1} seismic velocities observed at the bottom of 504B (1.8 km sub-basement; Alt *et al.* 1996). The lower resolution of the *Vp model*, which is capable of resolving velocity anomalies of 15 by 2 km as indicated by the checkerboard testing (Figs 5c,d), explains the slight misfit to the middle portion of the 504B sonic log (Fig. 5e), where only local seismic velocity structure is sampled.

Importantly, these models align with the lithological sampling of 504B, in which extrusive volcanics (0.0–0.6 km sub-basement) and sheeted dykes (0.8–1.8 km sub-basement) were cored. While these primary oceanic crustal lithologies were recovered, amphiboles and secondary hydrothermal mineralization were also observed, along with the inferred presence of porosity and fractures throughout the section. Together, these observations suggest that this ∼7-Myr-old oceanic crust has evolved through hydrothermal processes since its formation, but may also facilitate continued circulation as porosity remains open. How these properties vary along-profile will be discussed further and in greater detail within the context of additional geophysical models and geological sampling, to elucidate the controls on how the young CRR crust evolves over time.

9.1 Variations in Poisson's ratio

Poisson's ratio varies significantly both with distance from the CRR along SAP_B and with depth below basement (Fig. 9). Generally, σ is high in the uppermost crust and decreases with depth until *Vp* lies between 5.5 and 6.0 km s^{-1} which, when compared to previous investigations (Spudich & Orcutt 1980; Au & Clowes 1984; Bratt & Solomon 1984) occurs at a relatively slow velocity and shallow depth. The depth to which the high σ is observed along SAP_B is typically between 1.0 and 1.5 km sub-basement (Fig. 9d), significantly below the extrusive-intrusive transition (0.6–0.8 km), and well within the gabbroic dykes sampled by 504B (Detrick *et al.*

1994; Alt *et al.* 1996). At these depths, bulk porosity has significantly reduced from ∼15 per cent in the uppermost crust to <2 per cent, and continues to reduce below 0.9 km sub-basement (Pezard 1990; Alt *et al.* 1996). Laboratory-derived measurements of Poisson's ratio from the 504B core log reflect these changes in porosity, decreasing from the range of 0.28–0.32 in the upper 0.5 km sub-basement to 0.24–0.30 at ∼1.8 km depth sub-basement (Fig. 9d inset). The SAP_B Poisson's ratio-depth profile at 504B decreases from 0.29 at the basement to ∼0.24 at 1.2 km sub-basement, before increasing again to ∼0.26 by 2 km sub-basement. These measurements from the SAP_B seismic models broadly match the lower range of the laboratory-derived measurements, and are comparable to other profiles through young oceanic crust, further supporting the SAP_B Poisson's ratio model and reflecting the sensitivity of these different experimental methods to variations at sub-kilometre to sub-metre scales, respectively.

Below 1.0–1.5 km sub-basement along SAP_B, σ generally increases and, although there are no porosity measurements from 504B at these depths, Alt *et al.* (1996) observe significant increases in the proportion of amphibole and secondary mineralization deeper than 1.5 km below basement, with the associated alteration calculated to increase to 30–50 per cent by the base of 504B (1.8 km sub-basement). This increase in abundance of altered lithologies suggests that the remaining porosity at these depths becomes increasingly sealed through hydrothermally controlled secondary mineralization and recrystallization, and results in the observed return to Poisson's ratio measurements equivalent to laboratory samples of gabbro ($0.26 < \sigma < 0.28$; Christensen 2004) as observed along SAP_B (Fig. 9). This convergence to the measured Poisson's ratio of laboratory samples of gabbro supports the notions of Shaw (1994) and Christeson *et al.* (1997) that there are populations of varying aspect ratio cracks, and thus also σ, at different depths through the oceanic crust that are sealed as the oceanic crust ages. We also note that Poisson's ratio in the lower crust generally falls into one of two end members: lower values ($\sigma \approx 0.26$) and higher values ($\sigma \approx 0.30$–0.31). This division broadly correlates with sections of the profile where oceanic crust either formed at faster (>35 mm yr^{-1}) or slower (<35 mm yr^{-1}) FSR, respectively (Wilson *et al.* 2019). This suggests that lower crustal Poisson's ratio acts as a proxy to represent structural changes (increased tectonism), lithological differences (increased serpentinization), or both, inherited as a result of the dominant formation processes at the time of its formation.

9.2 CRR north flank lithology and structure—0–2 Ma

Immediately north of the CRR, both *Vp* and *Vs* are at their lowest (Figs 9b and c, respectively), with Poisson's ratio exceeding 0.31, the highest along profile (Fig. 9d). Previous studies (e.g. Peirce et al. 2019b, 2020) have interpreted a value of σ exceeding 0.31 ($Vp/Vs = 1.9$) to represent serpentinized mantle exhumed to the seabed, based on compilations of laboratory samples of oceanic rocks (Grevemeyer *et al.* 2018a and references therein). This proxy has been demonstrated to differentiate between mafic oceanic crust and serpentinized mantle both on and off-axis at the Mid-Cayman Spreading Centre (Grevemeyer *et al.* 2018a and Peirce *et al.* 2019b, respectively) as well as at the slow-spreading Mid-Atlantic Ridge (Peirce *et al.* 2020). At these lower spreading rates, the upper mantle temperature is cooler (Dick *et al.* 2003), and crustal formation is controlled increasingly by tectonic stretching instead of magmatic input (magmatic fraction, $M \leq 0.5$ – Buck *et al.* 2005). Thus, the low half-spreading rates (∼20 mm yr^{-1}) to the north of the CRR, combined with the consistently high Poisson's ratio ($\sigma > 0.31$), suggest that serpentinized lithologies are present to the north of the CRR, and thus the crust formed during a period dominated by tectonic spreading. However, the high degrees of spreading asymmetry at the CRR (Fig. 9a) obscure the observation that the full-spreading rate is, overall, ∼60 mm yr^{-1}, which lies towards the fast end of the intermediate spreading category (Dick *et al.* 2003).

Similar observations of high Poisson's ratio, exceeding the Grevemeyer *et al.* (2018a) threshold, are reported for young oceanic crust at spreading centres even within the fast spreading rate category. Collier & Singh (1998) report $\sigma \approx 0.48$ within the ∼100-m-thick Layer 2A at the East Pacific Rise (EPR), Spudich & Orcutt (1980) find σ to be more than 0.31 at <0.6 km sub-basement, and Bratt & Solomon (1984) report the same throughout the upper 4 km of EPR crust sampled. Although Shaw (1994) and Christeson *et al.* (1997) note that such high values of σ are not expected within typical oceanic crust, Shearer (1988) demonstrates that the combined effects of varying crack aspect ratio with anisotropy is sufficient to produce these higher values, even where porosity is present at very low percentages. Based on Shearer's (1988) modelling, and assuming a predominance of cracks running parallel to the spreading axis and, thus, perpendicular to SAP_B (e.g. Gregory 2018), the high Poisson's ratio determined throughout the upper crust of the CRR north flank may be caused by relatively high proportions of fractures and thin cracks (Shearer 1988) generated as the crust is accreted at lower spreading rates. Morphological evidence (Haughton *et al.* 2018) reveals little evidence of a predominance of tectonic extension on the northern flank of the CRR compared to the southern flank, although the seabed to the north is covered by pervasive lava flows that could post-date crustal formation at the ridge axis. Together, these observations support an interpretation of magma-dominated crustal accretion on the north flank of the CRR, in which the observed Poisson's ratio is a function of a high fracture and porosity density (Shearer 1988), such as that observed in the upper portion of young fast-spread EPR crust (Collier & Singh 1998), rather than as a result of metamorphosed lithologies at shallow crustal levels (e.g. Grevemeyer *et al.* 2018a; Peirce *et al.* 2020).

9.3 South flank lithology and structure—0–8 Ma

Between the CRR ridge axis and ∼40 km south of the CRR, crustal *Vs* is not resolved, due to a lack of observed *S*-wave arrivals (Figs 2 and 4), although *Vp* remains low and comparable to the north flank across these model offsets (Fig. 9). As distance increases south of the CRR both *Vp* and *Vs* generally increase, except for a region of lower velocity between 150 and 200 km (5–7 Myr), where the HSR was <30 mm yr^{-1} at the time of formation, with this long-wavelength variation reflected in a general decrease in Poisson's ratio across these offsets (from $\sigma \approx 0.31$ to $\sigma < 0.28$ – Fig. 9d). As with the north flank, these Poisson's ratio variations may be controlled by structural changes in the form of crustal porosity, or through differences in lithology as a result of varying degrees of serpentinization or hydrothermal mineralization.

The lack of significant regions where σ exceeds 0.31 on the south flank of the CRR suggests that it is unlikely, based on the Grevemeyer *et al.* (2018a) proxy, that serpentinized lithologies are present in significant volumes, and instead indicates that more typical oceanic crustal lithologies dominate this region of the model space. Further, changes in porosity, and in particular the sealing of fractures through mineralization (e.g. Shearer 1988; Wilkens *et al.* 1991), are typically associated with the ageing of oceanic crust,

as well as exhibiting strong controls on the Poisson's ratio (Shaw 1994; Christeson *et al.* 1997).

Although the Poisson's ratio variability may inform our understanding of each of these processes along profile, to differentiate between the likelihood and degree of control of these requires further information, including geological ground-truth from 504B combined with seismic anisotropy from the South Grid tomography survey, both of which are traversed by SAP_B (Fig. 1). Gregory (2018) undertook an anisotropy analysis of the South Grid data and showed that there is significant azimuthal anisotropy within the upper 2.5 km of the oceanic crust, with the fast direction aligned along 097°, subparallel with the abyssal hill (095°) and CRR (092°) strikes. In the uppermost 0.5 km, anisotropy is weak. However, from 0.5 to 1.5 km below basement the anisotropy in both *Vp* and *Vs* increases, reflecting the change from randomly orientated void spaces in the extrusive volcanics to the increasingly structured ridge-parallel orientations of the sheeted dykes (Gregory 2018). These results are supported by the inferred presence of large volumes of voids and fractures at 504B (Alt *et al.* 1996), and also align with observations from upper-dyke section depths of young EPR crust where seismic anisotropy is ∼4 per cent (Sohn *et al.* 2004). The evidence of hydrothermal mineralization and inferred porosity at 504B (Alt *et al.* 1996), together with the significant seismic anisotropy (Gregory 2018) indicates that while hydrothermal flow has reduced porosity in this 7-Myr-old CRR crust (Kolandaivelu *et al.* 2020), some fractures remain open.

With this ground-truth established for the uppermost portion (∼1.8 km) of the 7 Myr-old CRR crust, the general decrease in σ south along SAP_B likely represents the gradual closure of formational porosity and fractures as a result of hydrothermal circulation-enabled mineralization and alteration. These changes are supported by the contemporaneous increases in both compressional and shear wave seismic velocities, as well as density along SAP_B. Regions of anomalously low σ to the south of the CRR, notably at ∼95 and 200 km, likely represent localized modelling anomalies, associated with unusually high regions of *Vs*. Conversely, relatively increased σ ($\geq$0.30) around 150 km south are associated with low *Vs* and low densities in the *density model* (Fig. 8), correlating well with the lowest HSRs south of the CRR. Together this suggests that while fractures are being infilled with mineralization, resulting in the net reduction of Poisson's ratio along profile, segments of oceanic crust formed during periods of low HSR (Wilson *et al.* 2019), and thus under greater tectonic formational processes (Buck *et al.* 2005), continue to retain their inherited structure, and may be differentiated from oceanic crust formed with a higher magmatic fraction. At greater distances (ages) than that sampled by SAP_B, the differences between magmatic and tectonic-end member oceanic crust may become indistinguishable due to the infilling of fractures. However, tomographic imaging of Atlantic oceanic crust indicates that clear seismological differences remain even at ∼60–75 Myr (Davy *et al.* 2020).

9.4 Controls on the evolution of upper oceanic crust at the CRR

Poisson's ratio generally decreases with increasing offset from the CRR (Fig. 9). While geological structure and geophysical properties are commonly presented as a function of distance along profile, in regions where oceanic spreading rates vary significantly over time this may visually confuse underlying relationships. In Fig. 10, we present data from SAP_B as a function of age to remove any artificial stretching effects caused by the significant variability in spreading rate (ranging between ∼20 and >40 HSR mm yr^{-1} – Wilson & Hey 1995; Wilson *et al.* 2019), and to enable comparison with previous investigations into similarly young (<8 Myr) oceanic crust. The conversion to age from distance from ridge axis is made using the SAP_A half-spreading rate model of Wilson *et al.* (2019), as this is derived from shipboard magnetic data along a proximal profile to SAP_B, although we note a similar trend was determined for SAP_C, as well as in the model of Wilson & Hey (1995, Fig. 9a).

To consider how lithology and morphology evolve as the oceanic crust ages, the average Poisson's ratio is calculated for the uppermost 1 km sub-basement, representative of the extrusive volcanics and the transition to basaltic dykes (Shaw 1994; Salisbury *et al.* 1996; Wilson *et al.* 2019), and horizontally grouped into 0.25 Myr bins to highlight longer wavelength variations (Fig. 10c). This relationship demonstrates a decreasing Poisson's ratio in the uppermost crust with age, changing from $\sigma \approx 0.32$ in crust <1 Myr to predominantly between $0.26 < \sigma < 0.28$ in crust > 6 Myr, representing a linear gradient of ∼0.0084 Myr^{-1}. This trend [$y = -0.0084(\pm 0.0002)x + 0.328(\pm 0.002)$] is calculated using a least-squares method for all of the SAP_B upper crustal binned data, and is weighted by the standard deviation of the sample. Results from studies at other sites (Au & Clowes 1984; Bratt & Solomon 1984; Collier & Singh 1998) also match this trend, despite differences in experimental factors such as orientation relative to spreading direction. An increase in *Vp* along SAP_B has previously been demonstrated (Wilson *et al.* 2019); however, the consistently decreasing Poisson's ratio with age indicates that *Vs* increases at a relatively faster rate, most likely due to the sealing of fault and fracture-related porosity (e.g. Shaw 1994; Christeson *et al.* 1997). Such a decrease in porosity along profile is supported by the laterally variable *density model*, which shows a long wavelength trend of increasing density with distance (age) from the ridge axis.

It is also possible that the observed changes in Poisson's ratio are primarily controlled by spreading rate (e.g. Grevemeyer *et al.* 2018a), with higher values representing a greater degree of metamorphism of the oceanic crust formed at a predominantly magmatic spreading centre (e.g. White *et al.* 1992; Grevemeyer *et al.* 2018b). Using variations in *Vp* along SAP_B, Wilson *et al.* (2019) proposed a HSR of ∼35 mm yr^{-1} as the marker for distinguishing between whether the crust formed at the CRR under magmatic conditions at higher spreading rates ($M \approx 1$) or magma-dominated ($0.5 < M < 1$) at lower spreading rates (as defined by Buck *et al.* 2005). Fig. 10(c) indicates that there is a less clear relationship between Poisson's ratio in the upper crust and spreading rate alone, although there appears to be a tendency for σ to be higher at a given age if the spreading rate of formation is below 35 mm yr^{-1}. Calculation of the weighted least-squares line of best fit for the SAP_B upper crustal binned data for slow (<35 mm yr^{-1}) and fast (>35 mm yr^{-1}) HSRs gives $y = -0.0099(\pm 0.0003)x + 0.338(\pm 0.002)$ and $y = -0.0032(\pm 0.0005)x + 0.297(\pm 0.003)$, respectively. The threefold difference between the gradients for Poisson's ratio in the upper crust formed at slow (–0.0099 Myr^{-1}) and fast (–0.0032 Myr^{-1}) spreading rates suggests that spreading rate may be a significant control on Poisson's ratio in <8-Myr-old oceanic upper crust. It is worth noting, however, that there is an absence of samples for upper oceanic crust formed during faster periods of spreading (>35 mm yr^{-1}) at <1 Myr old along SAP_B, and that the imposition of a linear line of best fit for these sample sets is most likely an oversimplification of this temporal relationship even for the short span of oceanic crustal ages sampled by SAP_B. Despite the caveats, this demonstration that spreading rate, and not just age, has a significant

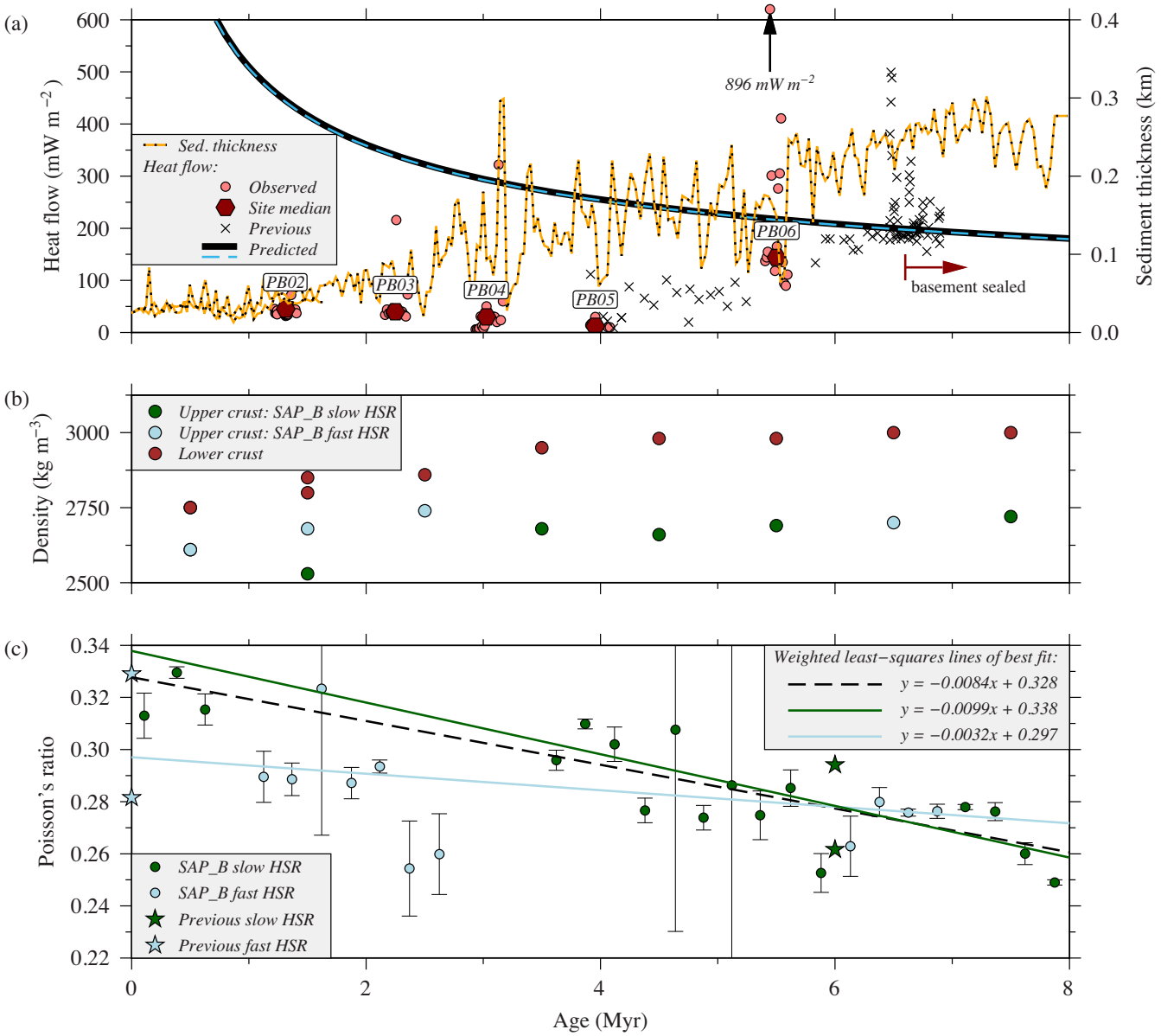

Figure 10. Variation in geological features and geophysical properties as a function of age along the SAP_B flowline profile from the CRR. (a) Observed conductive heat flow data and median values for each site from sampling along flowline as part of the OSCAR experiment (locations shown in Fig. 1b) and previous surveys (Kolandaivelu *et al.* 2020 and references therein), compared with the theoretical heat flow curves of Stein & Stein (1992 – black solid line) and Hasterok (2013 – blue dashed line). Overlain is the sediment thickness curve, determined from the SAP_B MCS data (Wilson *et al.* 2019). (b) Density variations in the upper and lower crust of the *density model* (Fig. 8c). (c) Poisson's ratio variation from the uppermost 1 km of the basement, averaged within 0.25 Myr bins to highlight the longer-wavelength trend, for model regions with data coverage. Error bars depict the one standard deviation used to represent variance and sample quality. Lines of best fit are calculated using a weighted least-squares method for all SAP_B binned data (dashed black line), SAP_B slow HSR-only binned data (dark green line) and SAP_B fast HSR-only binned data (light blue line). Note the threefold-steeper gradient of the line of best fit for the slow HSR-only samples compared to that for the fast HSR-only binned data. Results from previous studies at different spreading centres are also overlain (Au & Clowes 1984; Bratt & Solomon 1984; Collier & Singh 1998). Data in (b) and (c) are subdivided based on the flank-dependent HSR at the time of their formation into fast (>35 mm yr^{-1}) and slow (<35 mm yr^{-1}) categories. In all parts, annotation is shown in the keys.

correlation with Poisson's ratio in the upper 1 km of young oceanic crust supports the evidence from all *Vp* models along SAP_B (e.g. Fig. 9b) that the bulk porosity in the upper crust is increased due to tectonism associated with these lower spreading rates (Wilson *et al.* 2019). The variations in the *density model* further support these correlations, as density is modelled to be slightly raised in the upper 2 km of the crust in areas that were formed at higher spreading rates, implying reduced porosity, and is overlain on a long wavelength trend of increasing density with age observed in the upper and lower crust (Fig. 10b). The caveats associated with the weighted gradient calculated for the Poisson's ratio sets preclude further comment on the nature of the porosity and fractures, such as aspect ratio, that may fundamentally control these Poisson's ratio variations (e.g. Shearer 1988; Wilkens *et al.* 1991).

Over the 0–8 Myr period spanned by SAP_B, sediment thickness increases linearly by ~40 m Myr^{-1} to reach a thickness of ~275 m at 504B, excluding local variations controlled by basement faulting (Fig. 10a; Wilson *et al.* 2019). The extensive basement faulting and

sedimentation rate result in the crust not being fully 'sealed' until ∼7 Myr (Kolandaivelu *et al.* 2020), close to the location of 504B, where the conductive heat flow measurements intersect the predicted crustal heat flow curve (Stein & Stein 1992, 1994; Hasterok 2013). The observed decrease in Poisson's ratio, and thus interpreted reduction in porosity (Shearer 1988; Wilkens *et al.* 1991) spans this first 7 Myr of crustal evolution, suggesting that advective hydrothermal processes (Kolandaivelu *et al.* 2020) are sealing fractures on scales that our seismic refraction experiment is sensitive to. These processes appear to be active prior to the age at which the theoretical thermal sealing of the crust is achieved, although our profile does not extend far enough beyond this age to investigate how the fracture networks change once the basement is fully 'sealed' by sediment. Anomalously high heat flow measurements around 504B, where the theoretical curve is reached, suggests that there may be continued advective hydrothermal discharge (e.g. Kolandaivelu *et al.* 2020 and references therein) possibly facilitated through active or reactivated crustal faulting, as suggested by microseismicity observations (Tary *et al.* 2021), that disrupt and form fluid flow pathways through the sediment cover. The continued existence of such crustal permeability is inferred by borehole logging at 504B, and supported by significant seismic anisotropy observed within the South Grid (Gregory 2018). Irrespective of the mechanism by which the oceanic crustal porosity is being sealed, our results are consistent with and support heat flow studies of young oceanic crust (<10 Myr – Fisher *et al.* 2003), and other seismic velocity studies (<15 Myr – Audhkhasi & Singh 2019), that show significant evolution of the uppermost crust occurs within the first 10–15 Myr post-formation and, in the case of the CRR, within the first ∼7 Ma.

CONCLUSIONS

The short-wavelength structural variations within the upper oceanic crust formed at the CRR has been previously investigated through MCS imaging and the modelling of high-resolution *P*-wave data (Wilson *et al.* 2019). Our study extends this imaging through the crust and into the uppermost mantle by modelling of *P*- and *S*-wave traveltimes from OBSs. From the resulting *Vp* and *Vs* models, Poisson's ratio is calculated along profile, and provides new insight into variations in the lithology, alteration, and porosity. We interpret relationships between these models and the spreading rate to determine how formation and evolutionary processes control these properties at the CRR over the last ∼8 Myr. The results of our study indicate:

(i) S-wave phase arrivals are more widely observed in regions with smooth basement structure and significant sediment cover, resulting in regions of the *Vs model* and Poisson's ratio model where the crust is either not sampled or only poorly resolved. The majority of the *Vs model* is, however, sufficiently well resolved to investigate lateral (temporal) and vertical variations in structure. Variations in *Vs* correlate with variations in *Vp* along profile.

(ii) Poisson's ratio is high in the uppermost crust but decreases with depth towards the middle of the basaltic dyke sequence, correlating with a decrease in porosity measured in ODP borehole 504B. From the lower dyke sequence and into the gabbros, Poisson's ratio increases and, despite an absence of porosity measurements at these depths, most likely corresponds to an increase in secondary mineralization and alteration sampled at 504B, which suggests that any remaining fractures and porosity becomes increasingly sealed throughout these depths.

(iii) High Poisson's ratio, which modelling indicates pervades the oceanic crust immediately north of the CRR, is not atypical for recently formed crust at magma-dominated spreading ridges. Combined with geological evidence of magmatic processes and limited basement faulting, our models indicate that the high Poisson's ratio is most likely not caused by extensive metamorphism or deeper crust and uppermost mantle lithologies exhumed to shallower levels in the crust or to the seabed, but instead results from highly porous crust accreted through magma-dominated processes.

(iv) Along the south flank of the CRR, Poisson's ratio values are more typical of the oceanic crust, and broadly decrease with distance from the spreading centre. Superimposed on this long-wavelength variation, which is ground-truthed by existing borehole data and 3-D seismic anisotropy models, is evidence in the higher Poisson's ratio values that periods of low HSR retain the increased porosity and fracturing associated with the increased tectonism at the time of their formation.

(v) In the upper 1 km of the CRR crust, decreasing Poisson's ratio with age suggests that porosity is being progressively sealed from the time of its formation. Our modelling suggests that porosity is being sealed in the absence of significant sediment cover, and prior to the apparent thermal sealing at ∼7 Myr. As such, this study indicates that the early evolution of the CRR crust is controlled primarily by advective hydrothermal processes.

ACKNOWLEDGEMENTS

This research project was funded by the Natural Environment Research Council (NERC) grant NE/I027010/1. We would like to thank all those involved in the planning and acquisition of data during research cruises JC114 and SO238, including the officers, engineers and crew of the RRS James Cook and the FS Sonne, the scientific party and all seagoing NERC facility technicians and engineers. The NERC Ocean-Bottom Instrumentation Facility (Minshull *et al.*, 2005) provided the OBSs and their technical support at sea. Seismic data were processed and manipulated for plotting using Seismic Unix (Cohen & Stockwell, 2010). All figures were prepared using the Generic Mapping Tools (GMT) package (Wessel *et al*. 2013). Data from cruises JC114 and SO238 are archived at the NERC's British Oceanographic Data Centre, and the final accepted version of this manuscript is available through Durham Research Online (dro.dur.ac.uk). We thank our two anonymous reviewers for their positive and constructive comments.

REFERENCES

Alt, J.C., Kinoshita, H., Stokking, L.B. & Michael, P.J.(eds), 1996. *Proceedings of the Ocean Drilling Program, Sci. Results,* Vol. 148, College Station, TX.

Argus, D.F., Gordon, R.G. & DeMets, C., 2011. Geologically current motion of 56 plates relative to the no-net-rotation reference frame, *Geochem. Geophys. Geosys.,* **12**(11), 1–13.

Au, D. & Clowes, R.M., 1984. Shear-wave velocity structure of the oceanic lithosphere from ocean bottom seismometer studies, *Geophys. J. R. astr. Soc.,* **77,** 105–123.

Aubouin, J., Stephan, J.F., Renard, V., Roump, J. & Lonsdale, P., 1981. Subduction of the Cocos plate in the Mid America Trench, *Nature,* 294.

Audhkhasi, P. & Singh, S.C., 2019. Seismic structure of the upper crust from 0-75 Ma in the equatorial atlantic ocean on the african plate using ultra-long offset seismic data, *Geochem., Geophys., Geosys.,* **20,** 6140–6162.

Banyte, D., Morales Maqueda, M., Hobbs, R., Smeed, D.A., Megann, A. & Recalde, S., 2018a. Geothermal heating in the Panama Basin. Part I: hydrography of the basin, *J. geophys. Res.,* **123,** 7382–7392.

Banyte, D., Morales Maqueda, M., Smeed, D.A., Megann, A., Hobbs, R. & Recalde, S., 2018b. Geothermal heating in the Panama Basin. Part II: abyssal water mass transformation, *J. geophys. Res.,* **123,** 7393–7406.

Billen, M., Cowgill, E. & Buer, E., 2007. Determination of fault friction from reactivation of abyssal-hill faults in subduction zones, *Geology,* **35**(9), 819–822.

Bratt, S.R. & Solomon, S.C., 1984. Compressional and shear-wave structure of the East Pacific Rise at 11°20'N – constraints from 3-component ocean bottom seismometer data, *J. geophys. Res.,* **89,** 6095–6110.

Bown, J.W. & White, R.S., 1994. Variation with spreading rate of oceanic crustal thickness and geochemistry, *Earth planet. Sci. Lett.,* **121**(3-4), 435–449.

Buck, W.R., Carbotte, S.M. & Mutter, C., 1997. Controls on extrusion at mid-ocean ridges, *Geology,* **25,** 935–938.

Buck, W.R., Lavier, L.L. & Poliakov, A.N.B., 2005. Modes of faulting at mid-ocean ridges, *Nature,* **434,** 719–723.

Cann, J.R. *et al.*, 1997. Corrugated slip surfaces formed at ridge-transform intersections on the Mid-Atlantic Ridge, *Nature,* **385,** 329.

Carlson, R.L., 2010. How crack porosity and shape control seismic velocities in the upper oceanic crust: modeling downhole logs from Holes 504B and 1256D, *Geochem. Geophys. Geosys.,* **11**(4), 1–15.

Carlson, R. & Raskin, G., 1984. Density of the ocean crust, *Nature,* **311,** 555–558.

Carlson, R.L. & Miller, D.J., 1997. A new assessment of the abundance of serpentinite in the oceanic crust, *Geophys. Res. Lett.,* **24,** 457–460.

Christensen, N.I., 1996. Poisson's ratio and crustal seismology, *J. geophys. Res.,* **101**(B2), 3139–3156.

Christensen, N.I., 2004. Serpentinites, peridotites and seismology, *Int. Geol. Rev.,* **46**(9), 795–816.

Christensen, N.I. & Salisbury, M.H., 1975. Structure and constitution of the lower oceanic crust, *Rev. Geophys. Space Phys.,* **13,** 57–86.

Christeson, G.L., Shaw, P.R. & Garmany, J.D., 1997. Shear and compressional wave structure of the East Pacific Rise, *9°-10°N,* **102**(B4), 7821–7835.

Christeson, G.L., Reece, R.S., Kardell, D.A., Estep, J.D., Fedotova, A. & Goff, J.A., 2020. South Atlantic transect: variations in oceanic crustal structure at 31°S, *Geochem., Geophys., Geosys.,* **21,** doi:10.1029/2020GC009017.

Cleary, Z., Schwartz, D. M., Mittelstaedt, E. & Harpp, K., 2020. Dynamic magma storage at near-ridge hot spots: evidence from new Gala´pagos gravity data, *Geochem., Geophys., Geosys.,* **21,** doi:10.1029/2019GC008722.

Cohen, J.K. & Stockwell, J.W., 2010. CWP/SU: seismic Un∗ x Release No. 42: an open source software package for seismic research and processing, Center for Wave Phenomena, Colorado School of Mines.

Collier, J.S. & Singh, S.C., 1998. Poisson's ratio structure of young oceanic crust, *J. geophys. Res.,* **103**(B9), 20 981–20 996.

Collins, J.A., Purdy, M.G. & Brocher, T.M., 1989. Seismic velocity structure at deep sea drilling project site 504b, panama basin: evidence for thin oceanic crust, *J. geophys. Res.,* **94**(B7), 9283–9302.

Davy, R.G., Collier, J.S. & Henstock, T.J. The VoiLA Consortium, 2020. Wide-angle seismic imaging of two modes of crustal accretion in mature Atlantic Ocean crust, *J. geophys. Res.,* **125,** doi:10.1029/2019JB019100.

Detrick, R., Collins, J., Stephen, R. & Swift, S., 1994. In situ evidence for the nature of the seismic layer 2/3 boundary in oceanic crust, *Nature,* **370,** 288–290.

Dick, H.J.B., Lin, J. & Schouten, H., 2003. An ultraslow-spreading class of ocean ridge, *Nature,* **426,** 405–412.

Fisher, A.T., Davis, E.E., Hutnak, M., Spiess, V., Zühlsdorff, L., Cherkaoui, A. & Mottl, M.J., 2003. Hydrothermal recharge and discharge across 50 km guided by seamounts on a young ridge flank, *Nature,* **421**(6923), 618–621.

Fisher, A.T. & Von Herzen, R.P., 2005. Models of hydrothermal circulation within 106 ma seafloor: constraints on the vigor of fluid circulation and crustal properties, below the Madeira Abyssal Plain, *Geochem., Geophys., Geosys.,* **6,** Q11001, doi:10.1029/2005GC001013.

Fryer, G.J., Miller, D.J. & Berge, P., 1989. Seismic anisotropy and age-dependent structure of the upper oceanic crust, in *Evolution of Mid Ocean Ridges, Geophys. Monogr. Set.*, Vol. 57, ed. Sinton, J.M., pp. 1–8, AGU.

GEBCO Compilation Group. 2020. GEBCO 2020 Grid, doi:10.5285/a29c5465-b138-234d-e053-6c86abc040b9.

Gregory, E.P.M., 2018, The seismic characterisation of layer 2 in oceanic crust around ODP borehole 504B, *PhD thesis*, University of Durham, Durham.

Grevemeyer, I., Hayman, N.W., Peirce, C., Schwardt, M., Van Avendonk, H.J.A. & Dannowski, A., 2018a. Episodic magmatism and serpentinized mantle exhumation at an ultraslow-spreading centre, *Nature,* **11,** 444–448.

Grevemeyer, I., Ranero, C.R. & Ivandic, M., 2018b. Structure of oceanic crust and serpentinization at subduction trenches, *Geosphere,* **14**(2), 395–418.

Harding, J.L., Van Avendonk, H.J.A., Hayman, N.W., Grevemeyer, I., Peirce, C. & Dannowski, A., 2017. Magmatic-tectonic conditions for hydrothermal venting on an ultraslow-spread oceanic core complex, *Geology,* **45**(9), 839–842.

Hasterok, D., 2013. A heat flow based cooling model for tectonic plates, *Earth planet. Sci. Lett.,* **361,** 34–43.

Haughton, G.A., Hobbs, R., Murton, B. & Henstock, T., 2018. Spreading ridge lower order segmentations effect on large scale fault heave, Abstract EGU2018-15830, in *Presented at 2018 EGU General Assembly,* Vienna, April 8–13.

Hey, R., 1977. Tectonic evolution of the Cocos-Nazca spreading center, *Bull. geol. Soc. Am.,* **88**(10), 1404–1420.

Hobbs, R.W. & Peirce, C., 2015, RRS James Cook JC114 Cruise report.

Howell, S.M., Olive, J-A., Ito, G., Behn, M.D., Escartín, J. & Kaus, B., 2019. Seafloor expression of oceanic detachment faulting reflects gradients in mid-ocean ridge magma supply, *Earth planet. Sci. Lett.,* **516,** 176–189.

Iturrino, G.J., Christensen, N.I., Becker, K., Boldreel, L.O., Harvey, P.K.H. & Pezard, P., 1995. Physical properties and elastic constants of upper crustal rocks from core-log measurements in hole 504B, in *Proceedings of the Ocean Drilling Program, Sci. Results*, Vol. 137/140, pp. 273–291.

Ivandic, M., Grevemeyer, I., Berhorst, A., Flueh, E.R. & McIntosh, K., 2008, Impact of bending related faulting on the seismic properties of the incoming oceanic plate offshore of Nicaragua, *J. geophys. Res.,* **113,** B05410, doi:10.1029/2007JB005291.

Karato, S. & Becker, K., 1983. Porosity and hydraulic properties of sediments from the galapagos spreading center and their relation to hydrothermal circulation in the oceanic crust, *J. geophys. Res.,* **88**(B2), 1009–1017

Klitgord, K.D. & Mudie, J.D., 1974. The Galapagos Spreading Centre: a near-bottom geophysical survey, *Geophys. J. R. astr. Soc.,* **38,** 563–586.

Kolandaivelu, K.P., Harris, R.N., Lowell, R.P., Robinson, A.H., Wilson, D.J. & Hobbs, R.W., 2020. Evolution of heat flow, hydrothermal circulation and permeability on the young southern flank of the Costa Rica Rift, *Geophys. J. Int.,* **220,** 278–295.

Lonsdale, P. & Klitgord, K.D., 1978. Structure and tectonic history of the eastern Panama Basin, *Bull. geol. Soc. Am.,* **89**(7), 981–999.

Lowell, R.P. *et al.*, 2020. Magma-hydrothermal interactions at the Costa Rica Rift from data collected in 1994 and 2015, *Earth planet. Sci. Lett.,* **531,** doi:10.1016/j.epsl.2019.115991.

MacLeod, C.J., Searle, R.C., Murton, B.J., Casey, J.F., Mallows, C., Unsworth, S.C., Achenbach, K.L. & Harris, M., 2009. Life cycle of oceanic core complexes, *Earth planet. Sci. Lett.,* **287,** 333–344.

Minshull, T.A., Sinha, M.C. & Peirce, C., 2005. Multi-disciplinary subseabed geophysical imaging - a new pool of 28 seafloor instruments in use by the United Kingdom Ocean Bottom Instrument Consortium, *Sea Technol.,* **46,** 27–31.

Morales Maqueda, M.A., 2015. FS Sonne cruise SO238 Report.

Müller, R.D., Sdrolias, M., Gaina, C. & Roest, W.R., 2008. Age, spreading rates, and spreading asymmetry of the world's ocean crust, *Geochem. Geophys. Geosyst.,* **9,** Q04006, doi:10.1029/2007GC001743.

Peirce, C., Reveley, G., Robinson, A.H., Funnell, M.J., Searle, R.C., Simão, N.M., MacLeod, C.J. & Reston, T.J., 2019a. Constraints on crustal structure of adjacent OCCs and segment boundaries at 13°N on the Mid-Atlantic Ridge, *Geophys. J. Int.,* **217**(2), 988–1010.

Peirce, C., Robinson, A.H., Campbell, A.M., Funnell, M.J., Grevemeyer, I., Hayman, N.W., Van Avendonk, H.J.A. & Castiello, G., 2019b. Seismic investigation of an active ocean-continent transform margin: the interaction between the Swan Islands Fault Zone and the ultraslow-spreading Mid-Cayman Spreading Centre, *Geophys. J. Int.,* **219**(1), 159–184.

Peirce, C., Robinson, A.H., Funnell, M.J., Searle, R.C., MacLeod, C.J. & Reston, T.J., 2020. Magmatism versus serpentinization—crustal structure along the 13°N segment at the Mid-Atlantic Ridge, *Geophys. J. Int.,* **221**(2), 981–1001.

Perram, L.J. & Macdonald, K.C., 1994. An overlapping spreading centre at 87°30'W on the Galapagos Spreading Centre, *Earth planet. Sci. Lett.,* **121,** 195–211.

Pezard, P.A., 1990. Electrical properties of mid-ocean ridge basalt and implications for the structure of the upper oceanic crust in hole 504B, *J. geophys. Res.,* **95**(B6), 9237–9264.

Ranero, C.R., Morgan, J.P., McIntosh, K. & Reichert, C., 2003. Bending-related faulting and mantle serpentinization at the Middle America Trench, *Nature,* **425,** 367–373.

Reston, T.J. & Ranero, C.R., 2011. The 3-D geometry of detachment faulting at mid-ocean ridges, *Geochem. Geophys. Geosyst.,* **12,** Q0AG05, doi:10.1029/2011GC003666.

Robinson, A.H., Zhang, L., Hobbs, R.W., Peirce, C. & Tong, V.C.H., 2020. Magmatic and tectonic segmentation of the intermediate-spreading Costa Rica Rift—a fine balance between magma supply rate, faulting and hydrothermal circulation, *Geophys. J. Int.,* **222**(1), 132–152.

Salisbury, M.H., Christensen, N.I. & Wilkens, R.H., 1996. Nature of the layer 2/3 transition from a comparison of laboratory and logging velocities and petrology at the base of hole 504B, in *Proceedings of the Ocean Drilling Program, Sci. Results*, Vol. 148, eds Alt, J.C., Kinoshita, H., Stokking, L.B. & Michael, P.J., College Station, TX.

Sallarès, V. & Charvis, P., 2003. Crustal thickness constraints on the geodynamic evolution of the Galapagos Volcanic Province, *Earth planet. Sci. Lett.,* **214,** 545–559.

Shaw, P.R., 1994. Age variations of oceanic crust Poisson's ratio: inversion and a porosity evolution model, *J. geophys. Res.,* **99**(B2), 3057–3066.

Shearer, P.M., 1988. Cracked media, Poisson's ratio and the structure of the upper oceanic crust, *Geophys. J.,* **92,** 357–362.

Simão, N.M., Peirce, C., Funnell, M.J., Robinson, A.H., Searle, R.C., MacLeod, C.J. & Reston, T.J., 2020. Three-dimensional P-wave velocity structure of oceanic core complexes at 13°N on the Mid-Atlantic Ridge, *Geophys. J. Int.,* 1555–1579.

Smith, D.K., Cann, J.R. & Escartin, J., 2006. Widespread active detachment faulting and core complex formation near 13°N on the Mid-Atlantic Ridge, *Nature,* **443,** 440–444.

Sohn, R.A., Webb, S.C. & Hildebrand, J.A., 2004. Fine-scale seismic structure of the shallow volcanic crust on the east pacific rise at 9°50′N, *J. geophys. Res.,* **109,** B12104.

Spudich, P. & Orcutt, J., 1980. Petrology and porosity of an oceanic crustal site: results from wave form modeling of seismic refraction data, *J. geophys. Res.,* **85,** 1409–1433.

Stein, C.A. & Stein, S., 1992. A model for the global variation in oceanic depth and heat flow with lithospheric age, *Nature,* **359,** 123–129.

Stein, C.A. & Stein, S., 1994. Constraints on hydrothermal heat flux through the oceanic lithosphere from global heat flow, *J. geophys. Res.,* **99**(B2), 3081–3095.

Tary, J.B., Hobbs, R.W., Peirce, C., Lemes Lesmes, C. & Funnell, M.J., 2021. Local rift and intraplate seismicity reveal shallow crustal fluid-related activity and sub-crustal faulting, *Earth planet. Sci. Lett*.

Toomey, D., Purdy, G.M., Solomon, S.C. & Wilcock, W.S.D., 1990. The three-dimensional seismic velocity structure of the East Pacific Rise near latitude 9°30′ N, *Nature,* **347,** 639–645.

Von Herzen, R.P., 2004. Geothermal evidence for continuing hydrothermal circulation in older (>60 Ma) ocean crust, in *Hydrogeology of the Oceanic Lithosphere,* eds Davis, E.E. & Elderfield, H., pp. 414–450, Cambridge Univ. Press.

Van Avendonk, H.J.A., Harding, A.J., Orcutt, J.A. & McClain, J.S., 1998. A two-dimensional tomographic study of the Clipperton transform fault, *J. geophys. Res.,* **103**(B8), 17 885–17 899.

Wessel, P., Smith, W.H.F., Scharroo, R., Luis, J. & Wobbe, F., 2013. Generic mapping tools: improved version released, *EOS, Trans. Am. geophys. Un.,* **94**(45), 409–410.

White, R.S., McKenzie, D. & O'Nions, R.K., 1992. Oceanic crustal thickness from seismic measurements and rare earth element inversions, *J. geophys. Res.,* **97**(B13), 19 683–19 715.

Wilkens, R.H., Fryer, G.J. & Karsten, J., 1991. Evolution of porosity and seismic structure of upper oceanic crust: importance of aspect ratios, *J. geophys. Res.,* **96,** 17 981–17 995.

Wilson, D.J., Robinson, A.H., Hobbs, R.W., Peirce, C. & Funnell, M.J., 2019. Does intermediate spreading-rate oceanic crust result from episodic transition between magmatic and magma-dominated, faulting-enhanced spreading? – The Costa Rica Rift example, *Geophys. J. Int.,* **218,** 1617–1641.

Wilson, D.S. & Hey, R.N., 1995. History of rift propagation and magnetization intensity for the Cocos-Nazca spreading center, *J. geophys. Res.,* **100**(95), 10041.

Zelt, C.A., 1998. Lateral velocity resolution from three-dimensional seismic refraction data, *Geophys. J. Int.,* **135,** 1101–1112.

Zelt, C.A. & Barton, P.J., 1998. Three-dimensional seismic refraction tomography: a comparison of two methods applied to data from the Faeroe Basin, *J. geophys. Res.,* **103**(B4), 7187–7210.

Zelt, C.A. & Smith, R.B., 1992. Seismic traveltime inversion for 2-D crustal velocity structure, *Geophys. J. Int.,* **108**(1), 16–34.